

Suspensions of finite-size neutrally-buoyant spheres in turbulent duct flow

Walter Fornari^{1†}, Hamid Tabaei Kazerooni^{1,2}, Jeanette Hussong²
and Luca Brandt¹

¹Linné Flow Centre and Swedish e-Science Research Centre (SeRC), KTH Mechanics,
SE-10044 Stockholm, Sweden

²Ruhr-Universität Bochum, Chair of Hydraulic Fluid Machinery, Universitätsstraße 150, 44801
Bochum, Germany

(Received ?; revised ?; accepted ?. - To be entered by editorial office)

We study the turbulent square duct flow of dense suspensions of neutrally-buoyant spherical particles. Direct numerical simulations (DNS) are performed in the range of volume fractions $\phi = 0 - 0.2$, using the immersed boundary method (IBM) to account for the dispersed phase. Based on the hydraulic diameter a Reynolds number of 5600 is considered. We report flow features and particle statistics specific to this geometry, and compare the results to the case of two-dimensional channel flows. In particular, we observe that for $\phi = 0.05$ and 0.1 , particles preferentially accumulate on the corner bisectors, close to the duct corners as also observed for laminar square duct flows of same duct-to-particle size ratios. At the highest volume fraction, particles preferentially accumulate in the core region. For channel flows, in the absence of lateral confinement particles are found instead to be uniformly distributed across the channel. We also observe that the intensity of the cross-stream secondary flows increases (with respect to the unladen case) with the volume fraction up to $\phi = 0.1$, as a consequence of the high concentration of particles along the corner bisector. For $\phi = 0.2$ the turbulence activity is strongly reduced and the intensity of the secondary flows reduces below that of the unladen case. The friction Reynolds number increases with ϕ in dilute conditions, as observed for channel flows. However, for $\phi = 0.2$ the mean friction Reynolds number decreases below the value for $\phi = 0.1$.

Key words:

1. Introduction

Particle-laden turbulent flows are commonly encountered in many engineering and environmental processes. Examples include sediment transport in rivers, avalanches, slurries and chemical reactions involving particulate catalysts. Understanding the behavior of these suspensions is generally a difficult task due to the large number of parameters involved. Indeed, particles may vary in density, shape, size and stiffness, and when non-dilute particle concentrations are considered the collective suspension dynamics depends strongly on the mass and solid fractions. Even in Stokesian and laminar flows, different combinations of these parameters lead to interesting peculiar phenomena. In turbulence, the situation is further complicated due to the interaction between particles and vortical structures of different sizes. Hence, the particle behavior does not depend only on its

† Email address for correspondence: fornari@mech.kth.se

dimensions and characteristic response time, but also on the ratio among these and the characteristic turbulent length and time scales. The turbulence features are also altered due to the presence of the dispersed phase, especially at high volume fractions. Because of the difficulty of treating the problem analytically, particle-laden flows are often studied either experimentally or numerically. In the context of wall-bounded flows, the suspension dynamics has often been studied in canonical flows such as channels and boundary layers. However, internal flows relevant to many industrial applications typically involve more complex, non-canonical geometries in which secondary flows, flow separation and other non-trivial phenomena are observed. It is hence important to understand the behavior of particulate suspensions in more complex and realistic geometries. We will here focus on turbulent square ducts, where gradients of the Reynolds stresses induce the generation of mean streamwise vortices. These are known as Prandtl's secondary motions of the second kind (Prandtl 1963). The suspension behavior subjected to these peculiar secondary flows will be investigated, as well as the influence of the solid phase on the turbulence features.

As said, interesting rheological behaviors can be observed already in the Stokesian regime. Among these we recall shear-thinning and thickening, jamming at high volume fractions and the generation of high effective viscosities and normal stress differences (Stickel & Powell 2005; Morris 2009; Wagner & Brady 2009). Indeed, for these multi-phase flows the response to the local deformation rate is altered and the effective viscosity μ_e changes with respect to that of the pure fluid μ . Shear-thickening and normal stress differences are observed also in the laminar regime and are typically related to the formation of an anisotropic microstructure that arises due to the loss of symmetry in particle pair trajectories (Kulkarni & Morris 2008; Picano *et al.* 2013; Morris & Haddadi 2014). In general, the effective viscosity of a suspension, μ_e , has been shown to be a function of the particle Reynolds number Re_p , the Péclet number Pe (quantifying thermal fluctuations), the volume fraction ϕ and, relevant to microfluidic application, of the system confinement (Fornari *et al.* 2016a; Doyeux *et al.* 2016).

Another important feature observed in wall-bounded flows is particle migration. Depending on the particle Reynolds number Re_p , different types of migrations are observed. In the viscous regime, particles irreversibly migrate towards the centerline in a pressure-driven Poiseuille flow. Hence, particles undergo a shear-induced migration as they move from high to low shear rate regions (Guazzelli & Morris 2011; Koh *et al.* 1994). On the other hand, when inertial effects become important, particles are found to move radially away from both the centerline and the walls, towards an intermediate equilibrium position. Segre & Silberberg (1962) first observed this phenomenon in a tube and hence named it as the tubular pinch effect. This migration is mechanistically unrelated to the rheological properties of the flow and results from the fluid-particle interaction within the conduit. The exact particle focusing position has been shown to depend on the conduit-particle size ratio and on the bulk and particle Reynolds numbers (Matas *et al.* 2004; Morita *et al.* 2017). In square ducts the situation is more complex. Depending on the same parameters, the focusing positions can occur at the wall bisectors, along heteroclinic orbits or only at the duct corners (Chun & Ladd 2006; Abbas *et al.* 2014; Nakagawa *et al.* 2015; Kazerooni *et al.* 2017; Lashgari *et al.* 2017a).

Already in the laminar regime, the flow in conduits is altered by the presence of solid particles. Relevant to mixing, particle-induced secondary flows are generated in ducts, otherwise absent in the unladen reference cases as shown by Amini *et al.* (2012); Kazerooni *et al.* (2017). Interesting results are found also in the transition regime from laminar to turbulent flow. It has been shown that the presence of particles can either increase or reduce the critical Reynolds number above which the transition occurs. In

particular, transition depends upon the channel half-width to particle radius ratio h/a , the initial arrangement of particles and the solid volume fraction ϕ (Matas *et al.* 2003; Loisel *et al.* 2013; Lashgari *et al.* 2015).

In the fully turbulent regime, most studies have focused on dilute suspensions of heavy particles, smaller than the hydrodynamic scales, in channel flows. This is known as the one-way coupling regime (Balachandar & Eaton 2010) as there is no back-influence of the solid phase on the fluid. These kind of particles are found to migrate from regions of high to low turbulence intensities (turbophoresis) (Reeks 1983) and the effect is stronger when the turbulent near-wall characteristic time and the particle inertial time scale are similar (Soldati & Marchioli 2009). It was later shown by Sardina *et al.* (2011, 2012) that close to the walls particles also tend to form streaky particle patterns.

When the mass fraction is high, the fluid motion is altered by the presence of particles (two-way coupling regime) and it has been shown that turbulent near-wall fluctuations are reduced while their anisotropy is increased (Kulick *et al.* 1994). The total drag is hence found to decrease (Zhao *et al.* 2010).

Small heavy particles tend to accumulate in regions of high compressional strain and low swirling strength in turbulent duct flows, especially in the near-wall and vortex center regions (Winkler *et al.* 2004). Sharma & Phares (2006) showed that while passive tracers and low-inertia particles stay within the secondary swirling flows (circulating between the duct core and boundaries), high inertia particles accumulate close to the walls, mixing more efficiently in the streamwise direction. In particular, particles tend to deposit at the duct corners. More recently, Noorani *et al.* (2016) studied the effect of varying the duct aspect ratio on the particle transport. These authors considered a higher bulk Reynolds number than Sharma & Phares (2006) and found that in square ducts, particle concentration in the viscous sublayer is maximum at the centerplane. However, increasing the aspect ratio, the location of maximum concentration moves towards the corner as also the kinetic energy of the secondary flows increases closer to the corners.

In the four-way coupling regime, considering dense suspensions of finite-size particles in turbulent channel flows (with radius of about 10 plus units), it was instead found that the large-scale streamwise vortices are mitigated and that fluid streamwise velocity fluctuations are reduced. As the solid volume fraction increases, fluid velocity fluctuation intensities and Reynolds shear stresses are found to decrease, however particle-induced stresses significantly increase and this results in an increase of the overall drag (Picano *et al.* 2015). Indeed, Lashgari *et al.* (2014) identified three regimes in particle-laden channel flow, depending on the different values of the solid volume fraction ϕ and the Reynolds number Re , each dominated by different components of the total stress. In particular, viscous, turbulent and particle-induced stresses dominate the laminar, turbulent and inertial shear-thickening regimes. The effects of solid-to-fluid density ratio ρ_p/ρ_f , mass fraction, polydispersity and shape have also been studied by Fornari *et al.* (2016b, 2018); Lashgari *et al.* (2017b); Ardekani *et al.* (2017).

Recently, Lin *et al.* (2017) used a direct-forcing fictitious method to study turbulent duct flows laden with a dilute suspension of finite-size spheres heavier than the carrier fluid. Spheres with radius $a = h/10$ (with h the duct half-width) were considered at a solid volume fraction $\phi = 2.36\%$. These authors show that particles sedimentation breaks the up-down symmetry of the mean secondary vortices. This results in a stronger circulation that transports the fluid downward in the bulk center region and upward along the side walls similarly to what observed for the duct flow over a porous wall by Samanta *et al.* (2015). As the solid-to-fluid density ratio ρ_p/ρ_f increases, the overall turbulence intensity is shown to decrease. However, mean secondary vortices at the bottom walls

are enhanced and this leads to a preferential accumulation of particles at the face center of the bottom wall.

In the present work, we study the turbulence modulation and particle dynamics in turbulent square-duct flows laden with particles. In particular we consider neutrally-buoyant finite-size spheres with radius $a = h/18$ (where h is the duct-half width), and increase the volume fraction up to $\phi = 0.2$. We use data from direct numerical simulations (DNS) that fully describe the solid phase dynamics via an immersed boundary method (IBM). We show that up to $\phi = 0.1$, particles preferentially accumulate close to the duct corners as also observed for small inertial particles and for laminar duct flows laden with spheres of comparable h/a and ϕ . At the highest volume fraction, instead, we see a clear particle migration towards the core region, a feature that is absent in turbulent channel flows with similar ϕ . Concerning the fluid phase, the intensity of the secondary flows and the mean friction Reynolds number increase with the volume fraction up to $\phi = 0.1$. However, for $\phi = 0.2$ we find a strong reduction in the turbulence activity. The intensity of the secondary flows decreases below the value of the unladen reference case. In contrast to what observed for channel flow, the mean friction Reynolds number at $\phi = 0.2$ is found to be smaller than for $\phi = 0.1$. Hence, the contribution of particle-induced stresses to the overall drag is lower than what observed in a channel flow.

2. Methodology

2.1. Numerical Method

During the last years, various methods have been proposed to perform interface-resolved direct numerical simulations (DNS) of particulate flows. The state of art and the different principles and applications have been recently documented in the comprehensive review article by Maxey (2017). In the present study, the immersed boundary method (IBM) originally proposed by Uhlmann (2005) and modified by Breugem (2012) has been used to simulate suspensions of finite-size neutrally-buoyant spherical particles in turbulent square duct flow. The fluid phase is described in an Eulerian framework by the incompressible Navier-Stokes equations:

$$\nabla \cdot \mathbf{u}_f = 0 \quad (2.1)$$

$$\frac{\partial \mathbf{u}_f}{\partial t} + \mathbf{u}_f \cdot \nabla \mathbf{u}_f = -\frac{1}{\rho_f} \nabla p + \nu \nabla^2 \mathbf{u}_f + \mathbf{f} \quad (2.2)$$

where \mathbf{u}_f and p are the velocity field and pressure, while ρ_f and ν are the density and kinematic viscosity of the fluid phase. The last term on the right hand side of equation (2.2) \mathbf{f} is the localized IBM force imposed to the flow to model the boundary condition at the moving particle surface (i.e. $\mathbf{u}_f|_{\partial V_p} = \mathbf{u}_p + \boldsymbol{\omega}_p \times \mathbf{r}$). The dynamics of the rigid particles is determined by the Newton-Euler Lagrangian equations:

$$\rho_p V_p \frac{d\mathbf{u}_p}{dt} = \oint_{\partial V_p} \boldsymbol{\tau} \cdot \mathbf{n} dS \quad (2.3)$$

$$I_p \frac{d\boldsymbol{\omega}_p}{dt} = \oint_{\partial V_p} \mathbf{r} \times \boldsymbol{\tau} \cdot \mathbf{n} dS \quad (2.4)$$

where \mathbf{u}_p and $\boldsymbol{\omega}_p$ are the linear and angular velocities of the particle. In equations (2.3) and (2.4), $V_p = 4\pi a^3/3$ and $I_p = 2\rho_p V_p a^2/5$ represent the particle volume and moment of inertia, $\boldsymbol{\tau} = -p\mathbf{I} + \nu \rho_f (\nabla \mathbf{u}_f + \nabla \mathbf{u}_f^T)$ is the fluid stress tensor, \mathbf{r} indicates the distance

from the center of the particles, and \mathbf{n} is the unit vector normal to the particle surface $\partial\mathcal{V}_p$.

In order to solve the governing equations, the fluid phase is discretized on a spatially uniform staggered Cartesian grid using a second-order finite-difference scheme. An explicit third order Runge-Kutta scheme is combined with a standard pressure-correction method to perform the time integration at each sub-step. The same time integration scheme has also been used for the evolution of eqs. (2.3) and (2.4). For the solid phase, each particle surface is described by N_L uniformly distributed Lagrangian points. The force exchanged by the fluid on the particles is imposed on each l -th Lagrangian point. This force is related to the Eulerian force field \mathbf{f} by the expression $\mathbf{f}_{ijk} = \sum_{l=1}^{N_L} \mathbf{F}_l \delta_d(x_{ijk} - \mathbf{X}_l) \Delta V_l$, where ΔV_l is the volume of the cell containing the l -th Lagrangian point and δ_d is the regularized Dirac delta function δ_d . Here, \mathbf{F}_l is the force (per unit mass) at each Lagrangian point, and it is computed as $\mathbf{F}_l = (\mathbf{U}_p(\mathbf{X}_l) - \mathbf{U}_l^*)/\Delta t$, where $\mathbf{U}_p = \mathbf{u}_p + \boldsymbol{\omega}_p \times \mathbf{r}$ is the velocity at the lagrangian point l at the previous time-step, while \mathbf{U}_l^* is the interpolated first prediction velocity at the same point. An iterative algorithm with second order spatial accuracy is developed to calculate this force field. To maintain accuracy, eqs. (2.3) and (2.4) are rearranged in terms of the IBM force field,

$$\rho_p V_p \frac{d\mathbf{u}_p}{dt} = -\rho_f \sum_{l=1}^{N_L} \mathbf{F}_l \Delta V_l + \rho_f \frac{d}{dt} \int_{\mathcal{V}_p} \mathbf{u}_f dV \quad (2.5)$$

$$I_p \frac{d\boldsymbol{\omega}_p}{dt} = -\rho_f \sum_{l=1}^{N_L} \mathbf{r}_l \times \mathbf{F}_l \Delta V_l + \rho_f \frac{d}{dt} \int_{\mathcal{V}_p} \mathbf{r} \times \mathbf{u}_f dV \quad (2.6)$$

where \mathbf{r}_l is the distance between the center of a particle and the l -th Lagrangian point on its surface. The second terms on the right-hand sides are corrections that account for the inertia of the fictitious fluid contained within the particle volume. Particle-particle and particle-wall interactions are also considered. Well-known models based on Brenner's asymptotic solution (Brenner 1961) are employed to correctly predict the lubrication force when the distance between particles as well as particles and walls is smaller than twice the mesh size. Collisions are modelled using a soft-sphere collision model, with a coefficient of restitution of 0.97 to achieve an almost elastic rebound of particles. Friction forces are also taken into account (Costa *et al.* 2015). For more detailed discussions of the numerical method and of the mentioned models the reader is referred to previous publications (Breugem 2012; Picano *et al.* 2015; Fornari *et al.* 2016*b,c*; Lashgari *et al.* 2016).

Periodic boundary conditions for both solid and liquid phases are imposed in the stream-wise direction. The *stress immersed boundary method* is used in the remaining directions to impose the no-slip/no-penetration conditions at the duct walls. The stress immersed boundary method has originally been developed to simulate the flow around rectangular-shaped obstacles in a fully Cartesian grid (Breugem *et al.* 2014). In this work, we use this method to enforce the fluid velocity to be zero at the duct walls. For more details on the method, the reader is referred to the works of Breugem & Boersma (2005) and Pourquie *et al.* (2009). This approach has already been used in our group (Kazerooni *et al.* 2017) to study the laminar flow of large spheres in a squared duct.

2.2. Flow geometry

We investigate the turbulent flow of dense suspensions of neutrally-buoyant spherical particles in a square duct. The simulations are performed in a Cartesian computational domain of size $L_x = 12h$, $L_z = 2h$ and $L_y = 2h$ where h is the duct half-width and

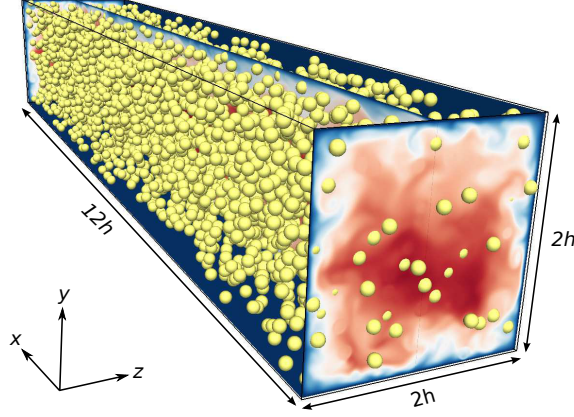


FIGURE 1. Instantaneous snapshot of the magnitude of the velocity together with the solid particles; the solid volume fraction $\phi = 0.1$.

x , y and z are the streamwise and cross-stream directions. The domain is uniformly ($\Delta x = \Delta z = \Delta y$) meshed by $2592 \times 432 \times 432$ Eulerian grid points in the streamwise and cross-flow directions. The bulk velocity of the entire mixture U_b is kept constant by adjusting the streamwise pressure gradient to achieve the constant bulk Reynolds number $Re_b = U_b 2h / \nu = 5600$. Based on the data provided by Pinelli *et al.* (2010), $Re_b = 5600$ corresponds to a mean friction Reynolds number $Re_\tau = \bar{U}_* h / \nu = 185$ for an unladen case, where $\bar{U}_* = \sqrt{\langle \tau_w \rangle / \rho_f}$ is the friction velocity calculated using the mean value of the shear stress τ_w along the duct walls.

We consider three different solid volume fractions of $\phi = 5, 10$ and 20% which correspond to 3340, 6680 and 13360 particles respectively. The reference unladen case is also considered for direct comparison. In all simulations, the duct-to-particle size ratio is fixed to $h/a = 18$, and the particles are randomly initialized in the computational domain with zero translational and angular velocities. The number of Eulerian grid points per particle diameter is 24 ($\Delta x = 1/24$) whereas the Lagrangian mesh on the surface of the particles consists of 1721 grid points.

The simulations start from the laminar duct flow and the noise introduced by a high amplitude localised disturbance in the form of two counter-rotating streamwise vortices (Henningson & Kim 1991). Due to this disturbance and to the noise added by the particles, transition naturally occurs at the chosen Reynolds number. The statistics are collected after the initial transient phase of about $100 h/U_b$, using an averaging period of at least $600 h/U_b$ (Huser & Biringen 1993; Vinuesa *et al.* 2014) (except for $\phi = 20\%$ where $\sim 400 h/U_b$ are found to be enough to obtain converged statistics). A summary of the simulations is presented in table 1 while an instantaneous snapshot showing the magnitude of the streamwise velocity for $\phi = 0.1$, together with the solid particles, is shown in figure 1.

3. Results

3.1. Validation

The code used in the present work has been already validated against several different cases in previous studies (Breugem 2012; Picano *et al.* 2015; Fornari *et al.* 2016c; Kazerooni *et al.* 2017). To further investigate the accuracy of the code, we calculate the friction

Case	$\phi = 0.0$	$\phi = 0.05$	$\phi = 0.1$	$\phi = 0.2$
N_p	0	3340	6680	13360
Re_b			5600	
$L_x \times L_y \times L_z$			$12h \times 2h \times 2h$	
$N_x \times N_y \times N_z$			$2592 \times 432 \times 432$	

TABLE 1. Summary of the different simulations cases. N_p indicates the number of particles whereas N_x , N_y and N_z are the number of grid points in each direction.

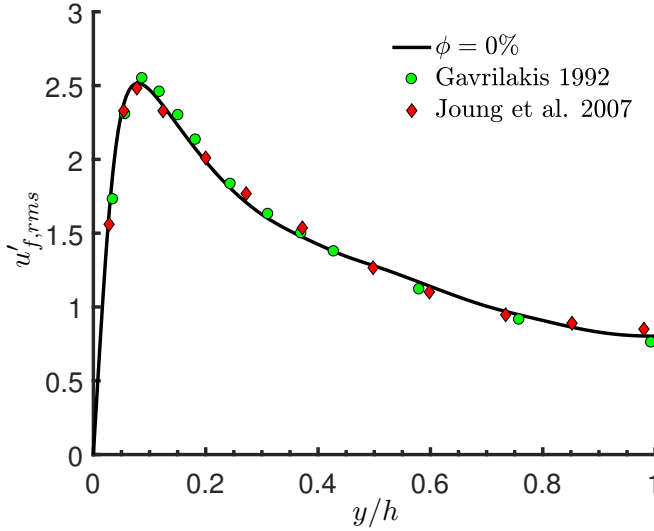


FIGURE 2. Streamwise velocity fluctuation at the wall-bisector from the present simulation at $Re_b = 4410$, and from the data by Gavrilakis (1992) at $Re_b = 4410$ and Joung *et al.* (2007) at $Re_b = 4440$.

factor $f = 8 (\bar{U}_*/U_b)^2$ for the reference unladen case with $Re_b = 5600$, and compare it with the value obtained from the empirical correlation by Jones (1976)

$$1/f^2 = 2\log_{10}(1.125Re_b f^{1/2}) - 0.8 \quad (3.1)$$

The same value of $f = 0.035$ is obtained from the simulation and the empirical formula. This corresponds to a mean $Re_\tau = 185$.

We also performed a simulation at lower $Re_b = 4410$ and $\phi = 0$, see figure 2, where we report the profile of the streamwise velocity fluctuation at the wall-bisector, normalized by the local friction velocity U_* . This is compared to the results by Gavrilakis (1992) and Joung *et al.* (2007) at $Re_b = 4410$ and 4440. We see a good agreement with both works.

3.2. Mean velocities, drag, and particle concentration

In this section we report and discuss the results obtained for the different solid volume fractions ϕ considered. The phase-ensemble averages for the fluid (solid) phase have been calculated by considering only the points located outside (inside) of the volume occupied by the particles. The statistics reported are obtained by further averaging over the eight symmetric triangles that form the duct cross section.

The streamwise mean fluid and particle velocities in outer units (i.e. normalized by the

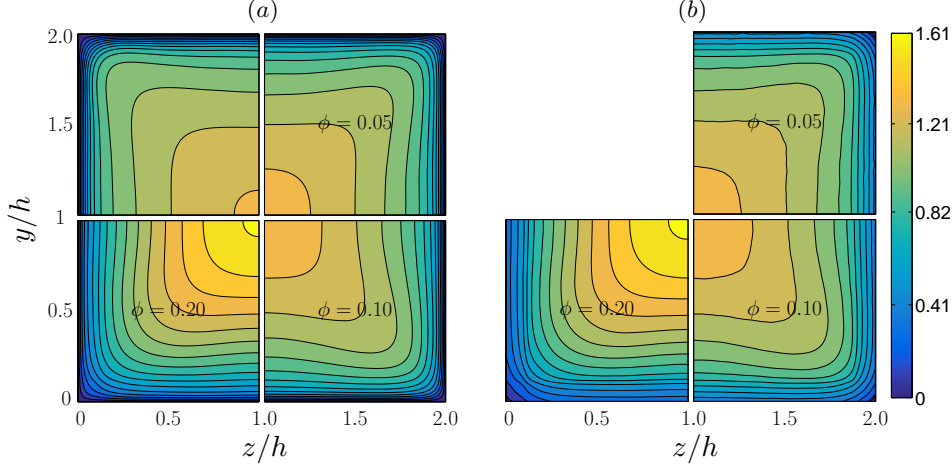


FIGURE 3. Contours of streamwise mean fluid (a) and particle velocity (b) in outer units. In each figure, the top-left, top-right, bottom-left and bottom-right quadrants show the data for $\phi = 0.0, 0.05, 0.1$ and 0.2 .

bulk velocity U_b), $U_{f/p}(y, z)$, are illustrated in figure 3(a,b) for all ϕ . The contour plots are divided in four quadrants showing results for $\phi = 0.0$ (top-left), 0.05 (top-right), 0.1 (bottom-right) and 0.2 (bottom-left). The streamwise mean particle velocity contours closely resemble those of the fluid phase. In particular we observe that the maximum velocity at the core of the duct grows with ϕ . The increase with ϕ is similar to that reported for turbulent channel flows (Picano *et al.* 2015), except for $\phi = 0.2$ where the increase of $U_{f/p}(y, z)$ in the duct core is substantially larger. We observe that the convexity of the mean velocity contours also increases with the volume fraction up to $\phi = 0.1$. This is due to the increased intensity of secondary flows that convect mean velocity from regions of large shear along the walls towards regions of low shear along the corner bisectors (Prandtl 1963; Gessner 1973; Vinuesa *et al.* 2014). For $\phi = 0.2$ the secondary flow intensity is substantially reduced and accordingly also the convexity of the contours of $U_{f/p}$ reduces.

Next, we show in figure 4(a) and (b) the streamwise mean fluid and particle velocity profiles along the wall-bisector in outer and inner units ($U_{f/p}(y)$ and $U_{f/p}^+(y^+)$). The local value of the friction velocity at the wall-bisector, $U_* = \sqrt{\tau_{w,bis}/\rho_f}$, is used to normalize $U_{f/p}(y)$. Solid lines are used for $U_f(y)$ while symbols are used for $U_p(y)$. We observe that the mean velocity profiles of the two phase are almost perfectly overlapping at equal ϕ , except very close to the walls ($y^+ \leq 30$) where particles have a relative tangential motion (slip velocity). Note also that the mean particle velocity decreases with ϕ very close to the walls. We also observe that by increasing ϕ , the profiles of $U_{f/p}(y)$ tend towards the laminar parabolic profile with lower velocity near the wall and larger velocity at the centerline, $y/h = 1$. Concerning $U_{f/p}^+(y^+)$, we observe a progressive downward shift of the profiles with the volume fraction ϕ denoting a drag increase, at least up to $\phi = 0.1$.

The mean-velocity profiles still follow the log-law (Pope 2000)

$$U_{f/p}^+(y^+) = \frac{1}{k} \log(y^+) + B \quad (3.2)$$

where k is the von Kármán constant and B is an additive coefficient. For the unladen case with $Re_b = 4410$, Gavrilakis (1992) fitted the data between $y^+ = 30$ and 100 to find

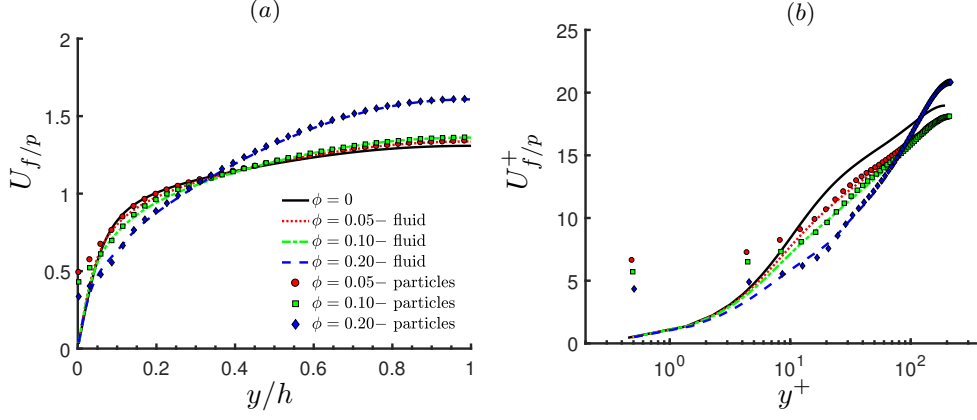


FIGURE 4. Streamwise mean fluid and particle velocity along the wall-bisector at $z/h = 1$ in outer (a) and inner units (b). Lines are used for fluid velocity profiles while symbols are used for particle velocity profiles.

Case	$\phi = 0.0$	$\phi = 0.05$	$\phi = 0.1$	$\phi = 0.2$
k	0.31	0.30	0.26	0.16
B	3.1	0.9	-1.6	-11.5
$Re_{\tau,bis}$	193	208	211	217
$Re_{\tau,mean}$	185	202	210	207
$Re_{\tau,2D}$	180	195	204	216

TABLE 2. The von Kármán constant and additive constant B of the log-law at the wall-bisector estimated from the present simulations for different volume fractions ϕ . Here k and B have been fitted in the range $y^+ \in [30, 140]$. The friction Reynolds number calculated at the wall-bisector $Re_{\tau,bis}$, the mean friction Reynolds number $Re_{\tau,mean}$ (based on $\langle \tau_w \rangle$, averaged over the walls), and the corresponding friction Reynolds number found by Picano *et al.* (2015) for turbulent channel flow, $Re_{\tau,2D}$, are also reported.

$k = 0.31$ and $B = 3.9$. In the present simulations, the extent of the log-region is larger due to the higher bulk Reynolds number and we hence fit our data between $y^+ = 30$ and 140. The results are reported in table 2. For the unladen case we obtain results in agreement with those of Gavrilakis (1992) although our constant B is slightly smaller. Increasing ϕ , k decreases and the additive constant B decreases becoming negative at $\phi = 0.1$. As shown by Virk (1975), the reduction in k should lead to drag reduction while the opposite effect is achieved by decreasing B .

The combinations of k and B pertaining our simulations correspond to an overall drag increase at the wall-bisector for increasing ϕ (as also shown for channel flows of comparable h/a and Re_b by Picano *et al.* 2015). To show this, we report in figure 5(a) and in table 2 the friction Reynolds number calculated at the wall-bisector, $Re_{\tau,bis}$ as function of the volume fraction ϕ . The results of Picano *et al.* (2015) are also reported for comparison in table 2. We see that although the initial value of $Re_{\tau,bis}$ for $\phi = 0.0$ is substantially larger than that of the corresponding channel flow at $Re_b = 5600$, the increase with the volume fraction is smaller in the duct. Indeed for $\phi = 0.2$ we find that $Re_{\tau,bis} \simeq Re_{\tau,2D}$. The increase in drag is hence less pronounced in square duct flow compared to the ideal channel flow case.

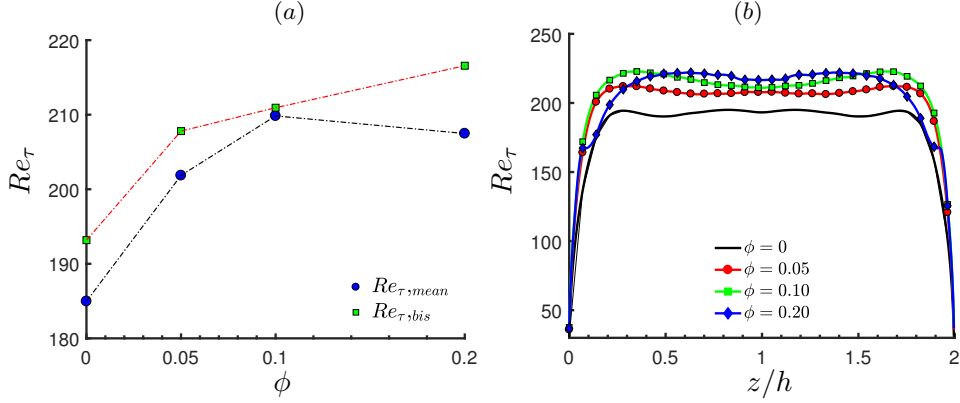


FIGURE 5. (a) Mean friction Reynolds number $Re_{\tau,mean}$ and friction Reynolds number at the wall bisector $Re_{\tau,bis}$ for different volume fractions ϕ . (b) Profile of Re_{τ} along the duct wall.

It is also interesting to observe the behavior of the mean friction Reynolds number $Re_{\tau,mean}$ as function of ϕ , as this directly relates to the overall pressure drop along the duct. From figure 5(a) and table 2 we see that it strongly increases with the volume fraction up to $\phi = 0.1$, while a reduction of $Re_{\tau,mean}$ takes place when ϕ is further increased. Observing the profiles of Re_{τ} along one wall (see figure 5b) we note that the friction Reynolds number increases with ϕ , especially towards the corners. For $\phi = 0.2$, however, the profile exhibits a sharp change at about $z/h = 0.1 \sim 2a$, and the maxima move towards the wall-bisector ($z/h \sim 0.65$). This is probably due to the clear change in local particle concentration in the cross-section as we will explain in the following.

The mean particle concentration over the duct cross-section $\Phi(y, z)$ is displayed in figure 6 for all ϕ , whereas the particle concentration along the wall-bisector ($z/h = 1$) and along a segment at $z/h = 0.2$ is shown in figure 7. Finally, we report in figure 8 the secondary (cross-stream) velocities of both phases, defined as $\sqrt{V_{f/p}^2 + W_{f/p}^2}$. We shall now discuss these 3 figures together.

Two interesting observations are deduced from figure 6: i) particle layers form close to the walls, and ii) for $\phi = 0.05$ and 0.1 , the local particle concentration $\Phi(y, z)$ is higher close to the duct corners. We have recently reported a similar result for laminar duct flow at $Re_b = 550$ and same duct-to-particle size ratio, $h/a = 18$, and volume fractions, ϕ (Kazerooni *et al.* 2017). At those Re_b and h/a , particles undergo an inertial migration towards the walls and especially towards the corners, while the duct core is fully depleted of particles. Clearly, turbulence enhances mixing and the depletion of particles at the duct core disappears. We believe that the higher particle concentration close to the corners is here related to the interaction between particles and secondary motion. Indeed, $\Phi(y, z)$ is lower at the wall-bisector, where the secondary flow is directed away from the wall, and higher where the cross-stream fluid velocity is directed towards the corners (see figure 8a). It is also interesting to observe that the presence of particles further enhances the fluid secondary flow around the corners for $\phi \leq 0.1$. This can be easily seen from figure 9, where both the maximum and the mean value of the secondary fluid velocity are shown as function of the volume fraction ϕ . The maximum value of the secondary cross-stream velocity increases from about 2% to 2.5% of U_b . The relative increase of the mean $\sqrt{V_f^2 + W_f^2}$ in comparison to the unladen case, is even larger than the increase in the maximum value at equal ϕ . Similarly, in laminar ducts, as particles migrate towards the corners, secondary flows are generated.

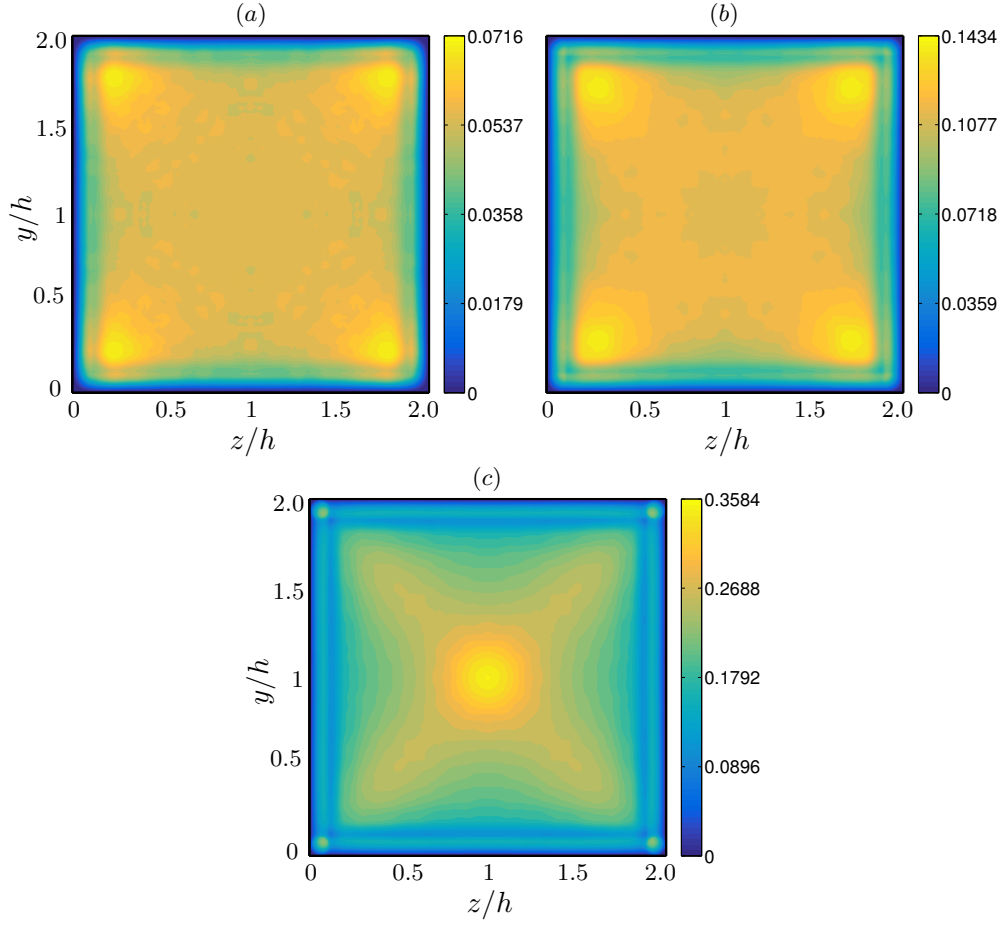


FIGURE 6. Mean particle concentration $\Phi(y, z)$ in the duct cross-section for $\phi = 0.05$ (a), $\phi = 0.1$ (b) and $\phi = 0.2$ (c).

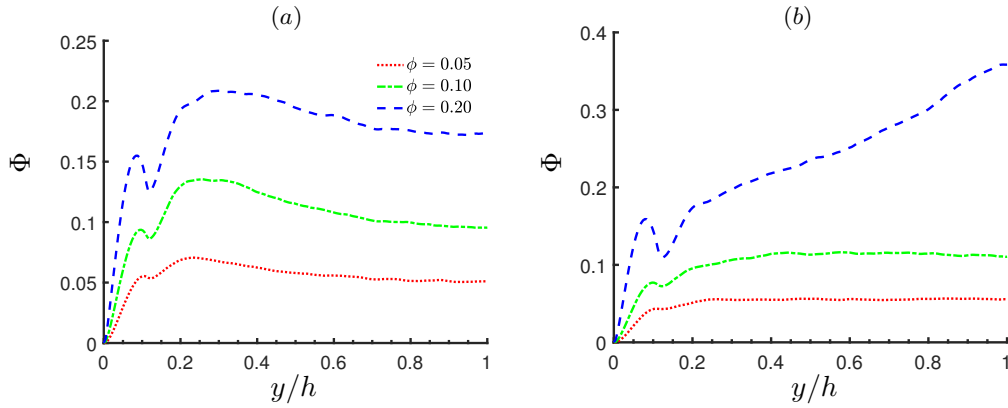


FIGURE 7. Mean particle concentration along a line at $z/h = 0.2$ and at the wall-bisector, $z/h = 1$.

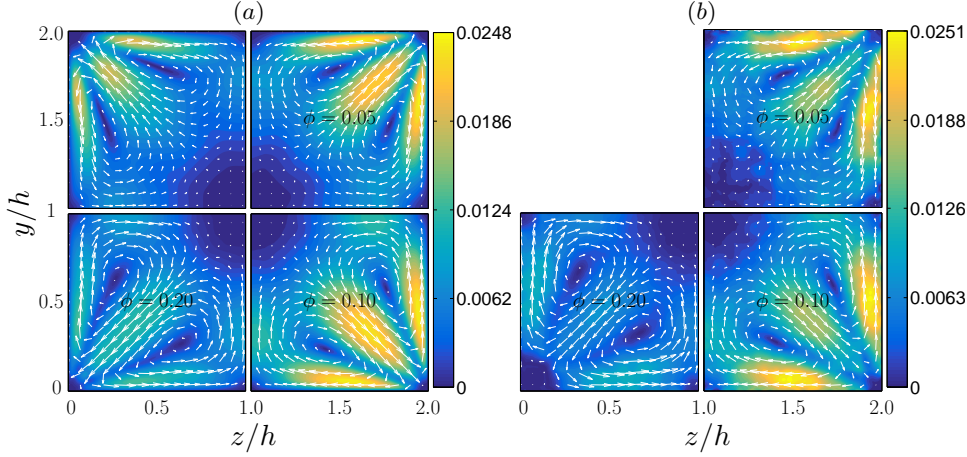


FIGURE 8. Contours and vector fields of the secondary flow velocity $\sqrt{V_{f/p}^2 + W_{f/p}^2}$ of the fluid (a) and solid phases (b).

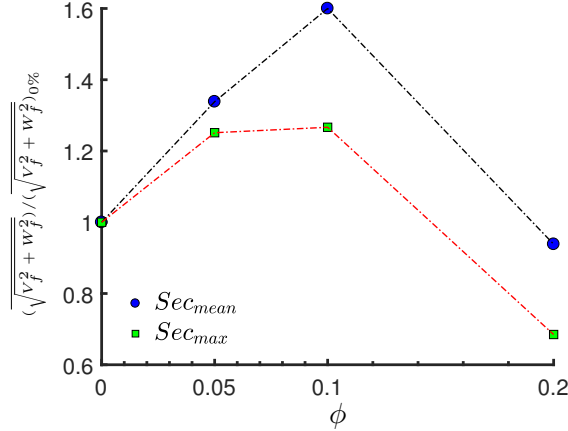


FIGURE 9. Mean and maximum value of the secondary flow velocity of the fluid phase as function of the solid volume fraction ϕ . Results are normalized by the values of the single-phase case.

As shown in figure 6, the particle concentration close to the corners increases with the volume fraction. However, the mean particle distribution in the cross-section changes at the highest volume fraction considered, $\phi = 0.2$: the highest values of $\Phi(y, z)$ are now found at the center of the duct (see figure 7b). This is not the case in turbulent channel flows and hence it can be related to the additional confinement of the suspension given by the lateral walls. As previously mentioned, the streamwise mean fluid and particle velocities are also substantially higher at the duct center for $\phi = 0.2$.

To better quantify this effect, we analyse the numerical data by Picano *et al.* (2015) and calculate the number of particles crossing the spanwise periodic boundaries per unit time h/U_b . For $\phi = 20\%$, we find that in 1 unit of h/U_b approximately 1% of the total number of particles cross the lateral boundaries. Inhibiting this lateral migration with lateral walls has therefore important consequences on the flow structure. We also calculated the probability density function of the particle centroid position along the spanwise direction. It is found that while the mean position is always at the channel center, $z/h = 1$, its variance grows in time as in a diffusive process. This is clearly not the case in a laterally

confined geometry.

Concerning the secondary fluid velocity (figure 8a), we note that for $\phi = 0.2$ both the maximum and the mean values decrease below those of the unladen case. The presence of the solid phase leads to an increase of the secondary fluid velocity, which however saturates for volume fractions between 0.1 and 0.2. As shown by these mean velocity profiles, the turbulence activity is substantially reduced at $\phi = 0.2$.

Vector and contour plots of the secondary motions of the solid phase are reported in figure 8(b). These closely resemble those of the fluid phase. However, the velocities at the corner-bisectors are almost half of those pertaining the fluid phase (in agreement with the fact that the particle concentration is high at this locations). Conversely, the cross-stream particle velocity is higher with respect to that of the fluid phase at the walls, close to the corners. For $\phi = 0.2$ we have previously noticed that along the duct walls, the highest particle concentration $\Phi(y, z)$ is exactly at the corners. In agreement, we also observe from figure 8(b) that the secondary particle velocity is negligible at these locations (i.e. particles tend to stay at these locations for long times).

3.3. Velocity fluctuations

Next, we report the contours of the root-mean-square (r.m.s.) of the fluid and particle velocity fluctuations in outer units, see figure 10. Due to the symmetry around the corner-bisectors, we show only the contours of $v'_{f/p,rms}(y, z)$ in panels (c) and (d). Corresponding r.m.s. velocities along two lines at $z/h = 0.2$ and 1 are depicted in figure 11. Results in inner units are shown at the wall-bisector, $z/h = 1$ in figure 12.

The contours of the streamwise fluid velocity fluctuations reveal that r.m.s. values are stronger near the walls (close to the wall-bisector), while minima are found along the corner bisectors. In this region, $u'_{f,rms}(y, z)$ is substantially reduced for $\phi = 0.2$, as also visible from the profiles in figure 11(a). From figure 11(a) we also see that the local maxima of $u'_{f,rms}(y)$ close to the corners is of similar magnitude for $\phi = 0.0, 0.05$ and 0.1. On the other hand, at the wall-bisectors the maxima of $u'_{f,rms}(y, z)$ decrease with ϕ , well below the value of the unladen case (see figure 11b). For $\phi = 0.2$ the profile of $u'_{f,rms}(y)$ deeply changes. In particular, the streamwise r.m.s. velocity $u'_{f,rms}(y)$ is substantially smaller than in the unladen case in the core region, where the particle concentration and the mean velocity are high while the secondary flows are negligible. After the maximum value, $u'_{f,rms}(y)$ initially decreases smoothly and then sharply for $y/h > 0.6$.

From figure 10(b) and figures 11(a,b) we see that the streamwise r.m.s. particle velocity, $u'_{p,rms}(y, z)$, resembles that of the fluid phase. However, $u'_{p,rms}(y, z)$ is typically smaller than $u'_{f,rms}(y, z)$ in the cross-section. Exceptions are the regions close to the walls where the particle velocity does not vanish (unlike the fluid velocity).

From the contour of $v'_{f,rms}(y, z)$ (see figure 10c), we see that r.m.s. velocities are larger in the directions parallel to the walls, rather than in the wall-normal direction. Close to the wall-bisectors, the peak values of the wall-normal and parallel fluid r.m.s. velocities increase with ϕ , again except for $\phi = 0.2$ when turbulence is damped. From figure 11(c) and (e) we see instead that close to the corners, the local maxima of both $v'_{f,rms}(y)$ (wall-normal) and $w'_{f,rms}(y)$ (wall-parallel) increase with respect to the unladen case, for all ϕ . At the wall-bisector (see figure 11d), wall-normal velocity fluctuations are slightly larger than the single-phase case for $\phi \lesssim 0.1$.

Finally, figure 11(f) shows profiles at the wall-bisector of the parallel component of the fluid velocity r.m.s, $w'_{f,rms}(y)$. Note that the peak value of $w'_{f,rms}(y)$ increases with the volume fraction up to $\phi = 0.1$ and moves closer to the wall. There is hence a clear redistribution of energy due to the particle presence towards a slightly more isotropic state.

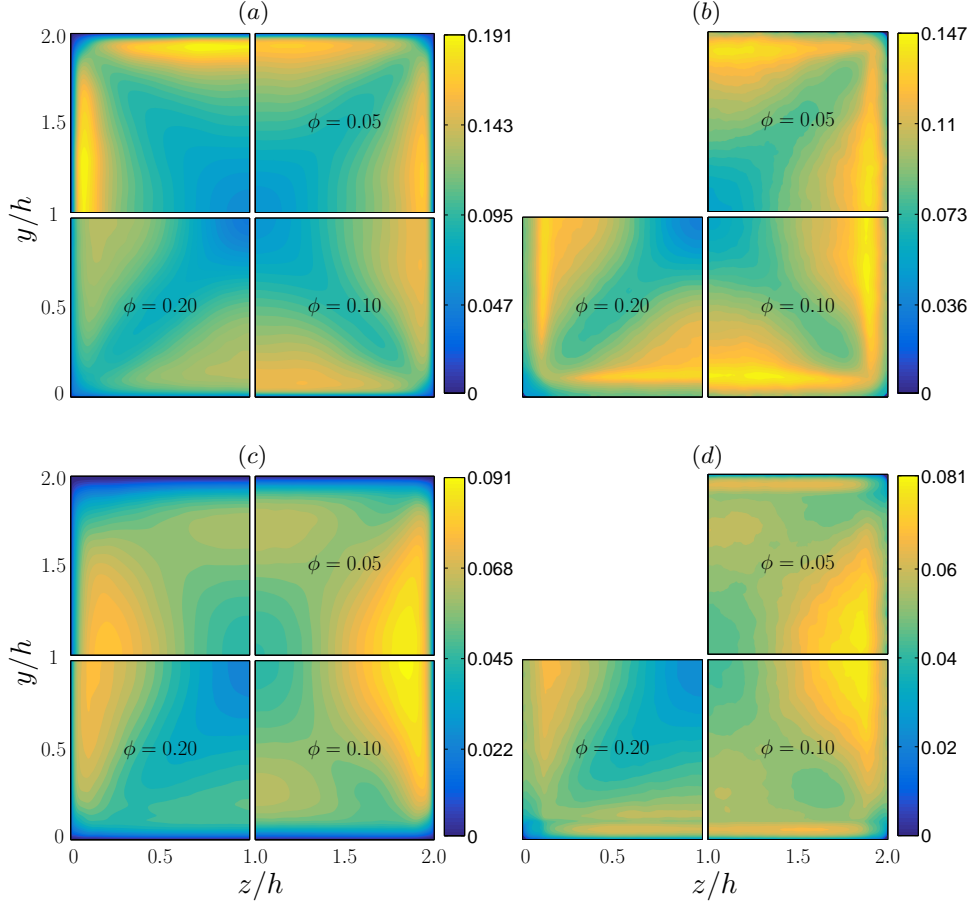


FIGURE 10. (a) Root-mean-square of the streamwise fluid velocity fluctuations in outer units, $u'_{f,rms}$, for all ϕ . (b) Root-mean-square of the streamwise particle velocity fluctuations in outer units, $u'_{p,rms}$, for all ϕ . (c) Root-mean-square of the vertical fluid velocity fluctuations in outer units, $v'_{f,rms}$, for all ϕ . (d) Root-mean-square of the vertical particle velocity fluctuations in outer units $v'_{p,rms}$, for all ϕ .

Concerning the solid phase, the wall-normal particle r.m.s. velocity, $v'_{p,rms}$, exhibits a peak close to the walls where particle layers form, see figures 10(d) and 11(d) (and also Costa *et al.* 2016). Differently from the channel flow analyzed by Picano *et al.* (2015), in the square duct flow $v'_{p,rms}$ decreases slowly with increasing volume fraction ϕ in the wall-particle layer ($y^+ \leq 20$) and the maxima are similar for all ϕ . This may be related to the existence of the secondary flows that pull the particles away from the walls towards the duct core. As for the fluid phase, the particle r.m.s. velocity parallel to the wall is greater than the perpendicular component close to the walls. From the profiles at the wall-bisector, see figure 11(f), we also see that the maximum of $w'_{p,rms}(y)$ is similar for $\phi = 0.05$ and 0.1, while it clearly decreases for the densest case simulated. More generally, we observe that particle r.m.s. velocities are similar to those of the fluid phase towards the core of the duct.

Both fluid and solid phase r.m.s. velocities are shown in inner units at the wall-bisector in figures 12(a,b,c). The local friction velocity has been used to normalize the velocity fluctuations. The fluid phase r.m.s. velocity increases with ϕ in the viscous sub-layer.

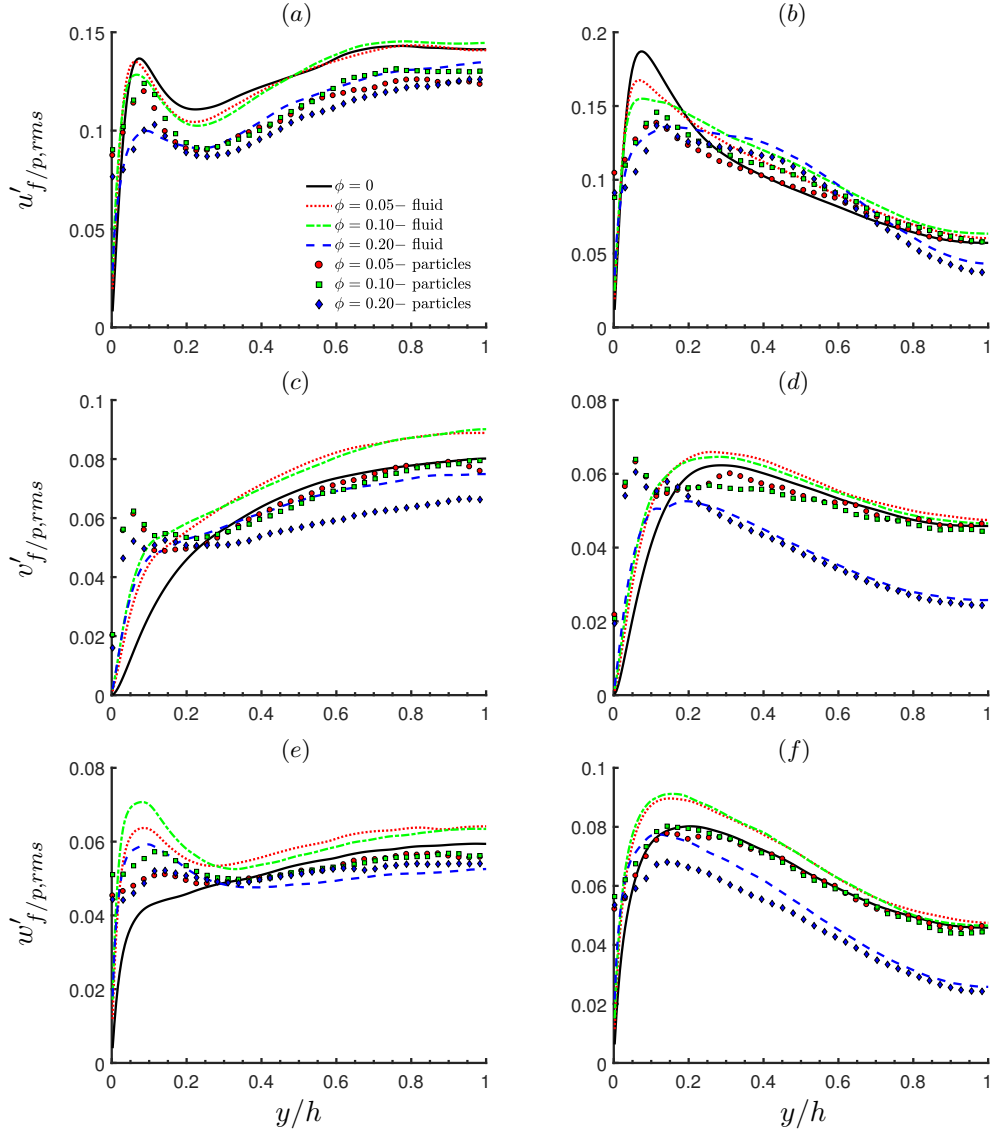


FIGURE 11. Root-mean-square of fluid and particle velocity fluctuations: (a),(b) streamwise, (c),(d) wall-normal and (e),(f) spanwise (z -direction) components in outer units at $z/h = 0.2$ (left column) and $z/h = 1$ (right column), for all ϕ . Lines and symbols are used for the fluid and solid phase statistics, respectively.

Clearly, the presence of solid particles introduces additional disturbances in the fluid increasing the level of fluctuations in regions where these are typically low (in the unladen case). On the other hand, particle velocity fluctuations are typically smaller than the corresponding fluid r.m.s. velocity, except in the inner-wall region, $y^+ < 20$, where they are one order of magnitude larger.

Finally, we also computed the mean turbulence intensity defined as $I = \langle u' \rangle / U_b$, with $u' = \sqrt{\frac{1}{3}(u_{f,rms}'^2 + v_{f,rms}'^2 + w_{f,rms}'^2)}$. This is shown in figure 13, where results are normalized by the value obtained for the unladen case. As for secondary flows, we see that the

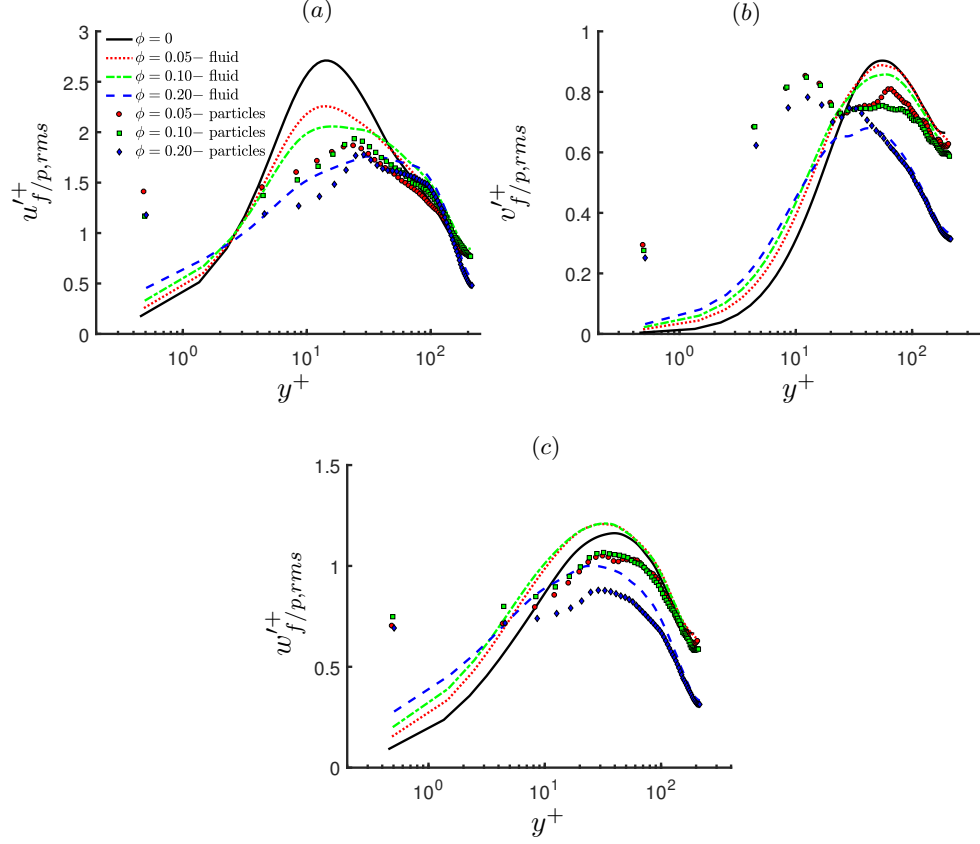


FIGURE 12. Root-mean-square of fluid and particle velocity fluctuations. (a) streamwise, (b) wall-normal and (c) spanwise (z -)direction components in inner units at $z/h = 1$ for all ϕ . Lines and symbols are used for the fluid and solid phase statistics as in figure 11.

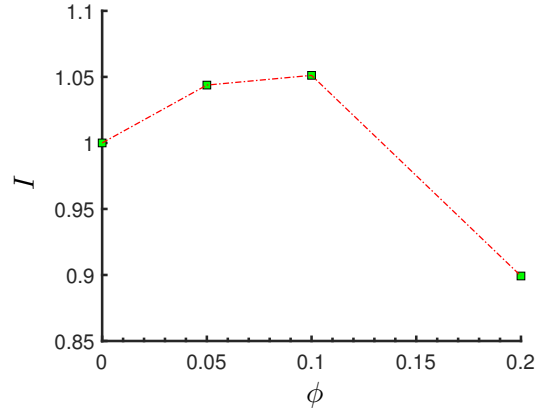


FIGURE 13. Mean turbulence intensity $I = \langle u' \rangle / U_b$ for all ϕ , normalized by the value for the unladen case.

turbulence intensity I increases up to $\phi = 0.1$, for which I is approximately 5% larger than the unladen value. For $\phi = 0.2$, instead, the mean turbulence intensity decreases well below the single-phase value, and $I(\phi = 0.2) \sim 0.9 I(\phi = 0)$.

3.4. Reynolds stress and mean fluid streamwise vorticity

We now turn to the discussion of the primary Reynolds stress in the duct cross-section, as this plays an important role in the advection of mean streamwise momentum. We show in figure 14(a) the $\langle u'_f v'_f \rangle$ component of the fluid Reynolds stress in the duct cross-section, for all ϕ . The component $\langle u'_f w'_f \rangle$ is not shown as it is the 90° rotation of $\langle u'_f v'_f \rangle$. We see that the maximum of $\langle u'_f v'_f \rangle$, located close to the wall-bisector, increases with the volume fraction up to $\phi = 0.1$. The maximum $\langle u'_f v'_f \rangle$ then progressively decreases with ϕ , denoting a reduction in turbulent activity. For $\phi = 0.2$ we observe that the maximum of $\langle u'_f v'_f \rangle$ reaches values even lower than in the unladen case. The contour of $\langle u'_f v'_f \rangle$ also changes with increasing ϕ . We find that $\langle u'_f v'_f \rangle$ increases towards the corners, and also for $\phi = 0.2$ it is larger than in the unladen case. However, the mean value of $\langle u'_f v'_f \rangle$ in one quadrant slightly increases up to $\phi = 0.1$, while for $\phi = 0.2$ the mean is 26% smaller than for the unladen case.

The profiles of $\langle u'_f v'_f \rangle$ at the wall-bisector ($z/h = 1$) are shown in figure 14(c). While the profiles for $\phi = 0.05$ and 0.1 are similar and assume larger values than the reference case, we see that for $\phi = 0.2$ the profile is substantially lower for all $z/h > 0.2$. This is also different to what found in channel flow as close to the core, $\langle u'_f v'_f \rangle$ is found to be similar for $\phi = 0.0$ and 0.2 . This is probably related to the high particle concentration at the duct core, see figure 6(c). Looking at the profiles in inner units, see figure 14(d), we also see that the peak values of $\langle u'_f v'_f \rangle^+$ are similar for the unladen case and for the laden cases with $\phi = 0.05$ and 0.1 . This is in contrast to what is found in channel flows, where a reduction of the peak with ϕ is observed (Picano *et al.* 2015). This shows that up to $\phi = 0.1$, the turbulence activity is not significantly reduced by the presence of particles. On the other hand, for $\phi = 0.2$ we observe a large reduction in the maximum $\langle u'_f v'_f \rangle^+$, denoting an important reduction in turbulent activity.

The Reynolds stress of the solid phase, $\langle u'_p v'_p \rangle$, is also shown for comparison in figures 14(b)-(d). The profiles are similar to those of the fluid phase, although $\langle u'_p v'_p \rangle < \langle u'_f v'_f \rangle$ for all ϕ , except close to the walls for $\phi = 0.2$. These local maxima may be related to the higher local particle concentration in layers close to the walls.

While for turbulent channel flow the cross-stream component of the Reynolds stress tensor, $\langle v'_f w'_f \rangle$, is negligible, in duct flow it is finite and contributes to the production or dissipation of mean streamwise vorticity. Hence it is directly related to the origin of mean secondary flows (Gavrilakis 1992; Gessner 1973). This can be seen from the Reynolds-averaged streamwise vorticity equation for a fully developed single-phase duct flow,

$$V_f \frac{\partial \Omega_f}{\partial y} + W_f \frac{\partial \Omega_f}{\partial z} + \frac{\partial^2 (\langle w_f'^2 \rangle - \langle v_f'^2 \rangle)}{\partial y \partial z} + \left(\frac{\partial^2}{\partial y^2} - \frac{\partial^2}{\partial z^2} \right) \langle v'_f w'_f \rangle - \nu \left(\frac{\partial^2}{\partial y^2} + \frac{\partial^2}{\partial z^2} \right) \Omega_f = 0 \quad (3.3)$$

where the mean vorticity

$$\Omega_f = \frac{\partial W_f}{\partial y} - \frac{\partial V_f}{\partial z}. \quad (3.4)$$

The first two terms of equation (3.3) represent the convection of mean vorticity by the secondary flow itself and have been shown to be almost negligible (Gavrilakis 1992). The third term is a source of vorticity in the viscous sublayer due to the gradients in the anisotropy of the cross-stream normal stresses. The fourth term, involving the secondary

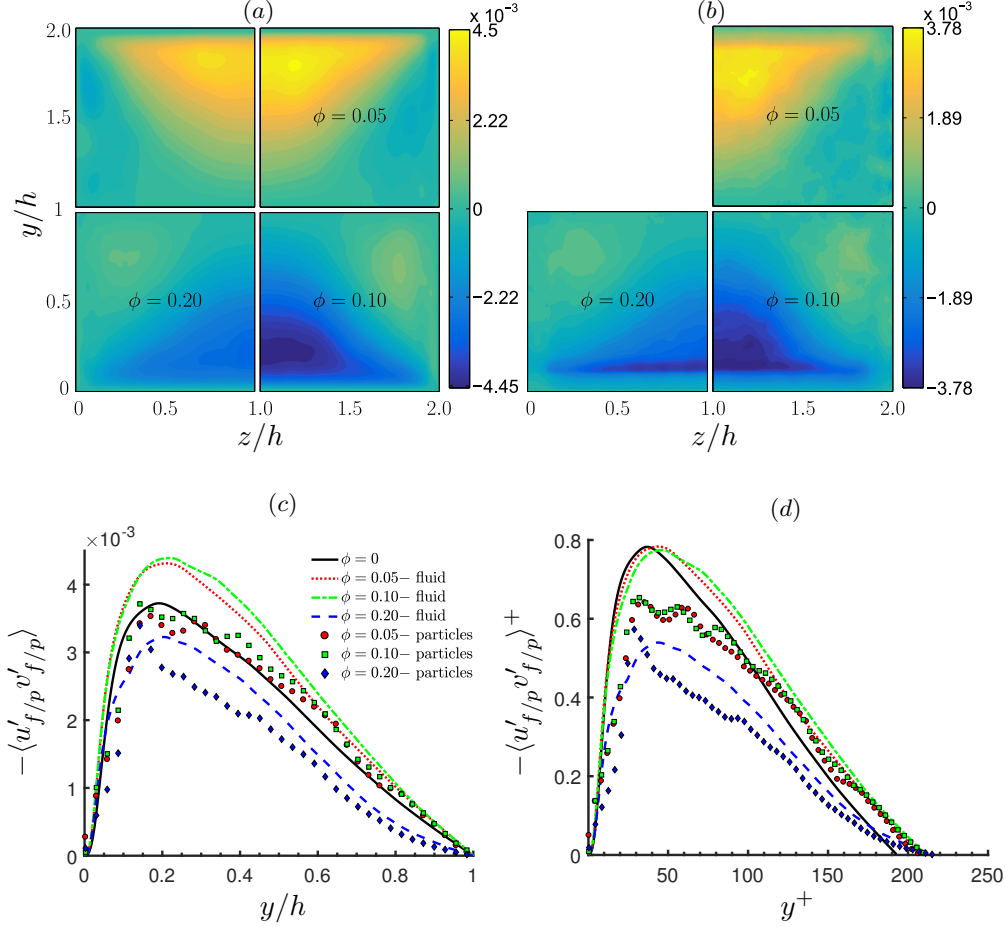


FIGURE 14. Contours of the primary Reynolds stress $\langle u'_{f/p} v'_{f/p} \rangle$ of (a) the fluid and (b) particle phase for all volume fractions considered. The profiles along the wall-bisector at $z/h = 1$ are shown in outer and inner units in panels (c) and (d). Lines and symbols are used for the fluid and solid phase statistics as in figure 11.

Reynolds stress, acts as source or sink of vorticity. Finally, the last term represents the viscous diffusion of vorticity.

The contours of $\langle v'_f w'_f \rangle$ are shown in figure 15 for all ϕ . These are non-negligible along the corner-bisectors (being directly related to mean secondary flows), and about one order of magnitude smaller than the primary Reynolds stress. Interestingly, we see that the maxima of $\langle v'_f w'_f \rangle$ strongly increases with ϕ up to $\phi = 0.1$ and also for $\phi = 0.2$, the maximum value is still larger than that for $\phi = 0.05$. We also notice that regions of finite $\langle v'_f w'_f \rangle$ become progressively broader with increasing ϕ .

The secondary Reynolds stress of the solid phase, $\langle v'_p w'_p \rangle$, resembles qualitatively that of the fluid phase, except at the corners where a high value of opposite sign is encountered. As a consequence, close to the corners this term may contribute in opposite way to the production or dissipation of vorticity with respect to $\langle v'_f w'_f \rangle$.

We conclude this section by showing in figure 16 the mean streamwise fluid vorticity Ω_f for all ϕ . The region of maximum vorticity at the wall is found between $z/h = 0.2$ and $z/h = 0.5$ for the unladen case and it extends closer to the corner for increasing ϕ .

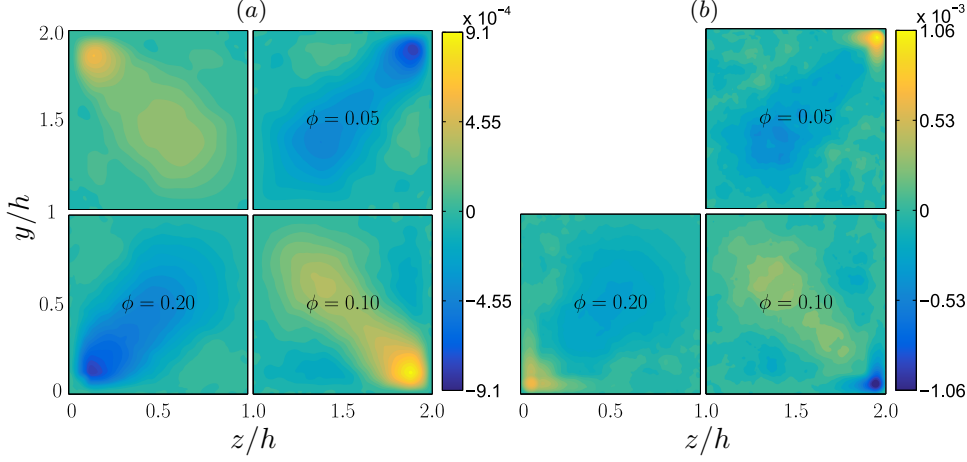


FIGURE 15. Contours of the secondary Reynolds stress $\langle v'_{f/p} w'_{f/p} \rangle$ of (a) the fluid and (b) the particle phase for all volume fractions ϕ under investigation.

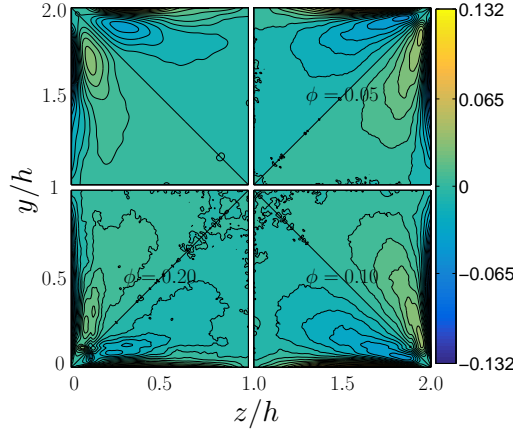


FIGURE 16. Contours of the mean fluid streamwise vorticity Ω_f for all ϕ under investigation.

We also find that the maximum Ω_f initially increases with the solid volume fraction (for $\phi = 0.1$ the maximum Ω_f is just slightly smaller than for $\phi = 0.05$). This is expected as also the intensity of the secondary motions increase. The contours of Ω_f become more noisy for $\phi = 0.2$, with a maximum value below that of the single-phase case. Also, for $\phi = 0.2$ the location of maximum Ω_f is similar to that found for the unladen case.

The mean streamwise vorticity changes sign further away from the walls. For the unladen case, the magnitude of the maximum vorticity at the walls is 2.5 times larger than the magnitude of the maximum vorticity of opposite sign found closer to the corner-bisector. As reference and for clarity, we will consider the vorticity to be positive at the wall, and negative further away, as found for the top and bottom walls (for the lateral walls the situation is reversed). We find that the vorticity minimum approaches progressively the walls as ϕ increases up to $\phi = 0.1$, and that the ratio between the magnitudes of the maximum and minimum of vorticity increases up to ~ 3 . On the other hand, for $\phi = 0.2$ we clearly notice several local vorticity minima. One minimum is further away from the walls, at a location similar to what found for the unladen case. Another minimum is further away towards the corner bisector. The other minimum is

instead close to the corners. As we have previously shown, at the largest ϕ there is a significant mean particle concentration exactly at the corners and correspondingly we see two intense spots of vorticity around this location, antisymmetric with respect to the corner-bisector.

Although equation (3.3) is valid for single-phase duct flow, we have calculated the convective, source/sink and diffusive terms for the cases of $\phi = 0, 0.05$ and 0.1 . For $\phi = 0.2$ there is a strong coupling between the dynamics of both fluid and solid phases, and it is therefore difficult to draw conclusions only by estimating the terms in equation (3.3).

As discussed by Gavrilakis (1992), the production of vorticity within the viscous sub-layer is the main responsible for the presence of vorticity in the bulk of the flow. The main contribution to the production of vorticity is given by the term involving the gradients of the cross-stream normal stresses. For the unladen case, the maxima of this term are located close to the corners (at $y/h = 0.016$, $z/h = 0.16$ from the bottom-left corner, similarly to what found by Gavrilakis 1992). Another positive, almost negligible contribution to the production of mean streamwise vorticity is given by the convective term. On the other hand, the diffusive term and the term involving the gradients of the secondary Reynolds stress give a negative contribution to the generation of vorticity in this inner-wall region. Note that the largest negative contribution due to the latter term is found close to the maximum production ($(y/h, z/h) = (0.016, 0.15)$ for $\phi = 0$). Generally, we observe that the maximum production and dissipation increase and approach the corner as the volume fraction increases up to $\phi = 0.1$ (not shown). In order to understand how the presence of particles contributes to the generation of vorticity, we calculate the ratio between the overall production and dissipation at the location of the maximum of the normal stress term (i.e. the summation of the convective term and the normal stress term, divided by the absolute value of the summation between the diffusive and secondary Reynolds stress terms). For the unladen case we have a good balance and the ratio is approximately 1. For $\phi = 0.05$ and 0.1 , the ratio is 0.96 and 0.95. Hence, the presence of the solid phase gives an additional contribution of about 5% to the generation of mean streamwise vorticity in the near-wall region at the location of maximum production. The increased production due to larger gradients of the normal stress difference and due to the additional contribution by particles, leads globally to the larger Ω_f observed at $\phi = 0.05$ and 0.1 .

3.5. Quadrant analysis and two-point velocity correlations

In this section we employ the quadrant analysis to identify the contribution from so-called ejection and sweep events to the production of $\langle u'_f v'_f \rangle$ and $\langle u'_f w'_f \rangle$. In single-phase wall-bounded turbulent flows, it is known that these phenomena are associated to pairs of counter-rotating streamwise vortices that exist in the shear layer near the wall. These force low-momentum fluid at the wall towards the high-speed core of the flow. This is typically referred to as a Q2 or ejection event, with negative u'_f and positive v'_f . On the other hand, events with positive u'_f and negative v'_f are associated with the inrush of high-momentum fluid towards the walls and are known as sweeps or Q4 events. Events Q1 (positive u'_f and positive v'_f) and Q3 (negative u'_f and negative v'_f) are not associated with any particular turbulent structure when there is only one inhomogeneous direction. However, as discussed by Huser & Biringen (1993) in turbulent duct flows these also contribute to the total turbulence production.

We first show contours of the probability of finding Q1, Q2, Q3, Q4 events for $\phi = 0.0$ and 0.05 in figure 17, and for $\phi = 0.1$ and 0.2 in figure 18. The maximum probability of an event is 1, so that the sum $Q1+Q2+Q3+Q4=1$ at each point. Since these events are typically important close to the walls, the y -coordinate is reported in inner units (the

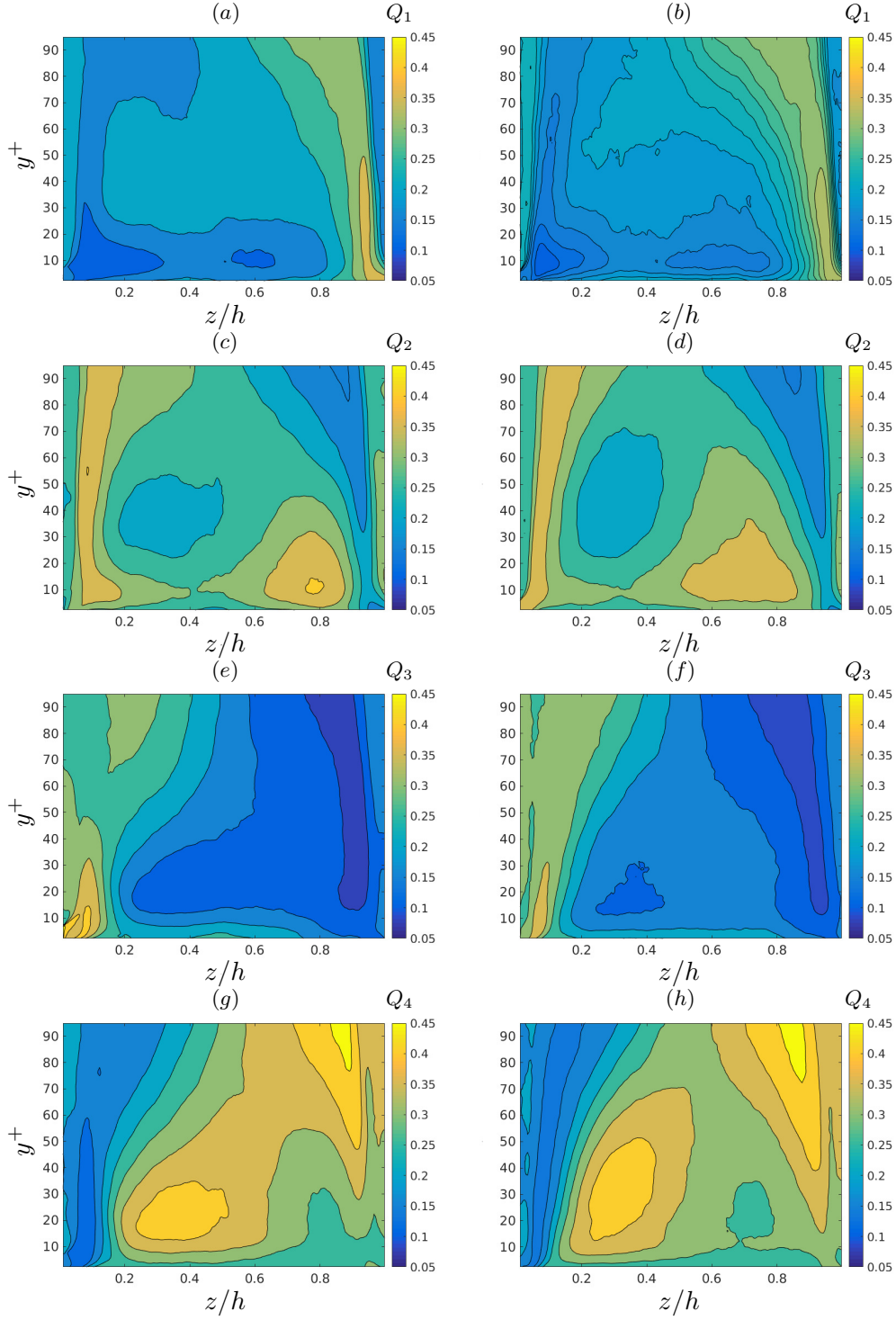


FIGURE 17. Maps of probability of Q1, Q2, Q3, Q4 events in panels (a), (c), (e), (g) and (b), (d), (f), (h) for particle volume fractions $\phi = 0.0$ and 0.05 , respectively.

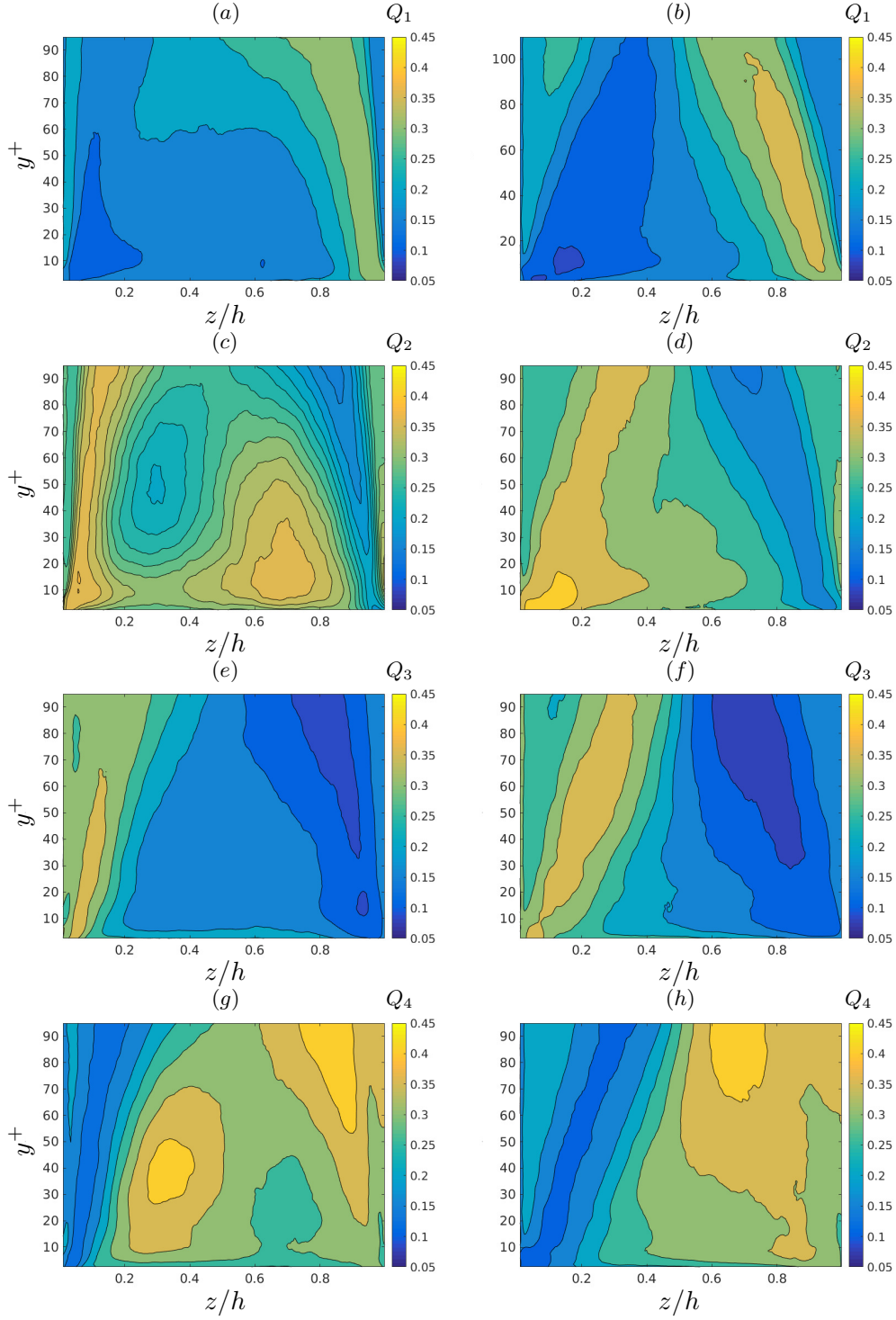


FIGURE 18. Maps of probability of Q_1, Q_2, Q_3, Q_4 events in panels (a), (c), (e), (g) and (b), (d), (f), (h) for particle volume fractions $\phi = 0.1$ and 0.2 , respectively.

viscous length at the wall-bisector is chosen), while the wall-parallel z -coordinate spans half of the duct. The contours of the probability of the different events directly enables us to easily compare and discuss all cases.

Results for the unladen case are substantially in agreement with those by Huser & Biringen (1993) and Joung *et al.* (2007). Ejection (Q2) events are important at the wall-bisector ($y/h = 1$) and around $y/h \sim 0.8$. Joung *et al.* (2007) report strong Q2 events already $y/h = 0.62$, and this is probably due to the fact that their Re_b was smaller than ours ($Re_b = 4410$ instead of 5600). Q4 events are instead dominant closer to the vertical walls, around $y/h = 0.3$ (as also reported by Joung *et al.* 2007). Q3 events are found when both u'_f and v'_f are negative. As also shown by Huser & Biringen (1993), we see that these increase from the wall-bisector towards the vertical walls, being dominant at the corners. Consequently, these events are created by ejections from the vertical wall (and particularly from the corners), resulting in the increase of $\langle u'_f v'_f \rangle$ in this region.

The general picture is similar for $\phi = 0.05$ and 0.1 . The probability maps of Q1, Q2, Q3 and Q4 events are only slightly changed with respect to those of the unladen case. Concerning the probability of Q3 events we see that it is still higher at the corner and that it increases with ϕ along the vertical wall and along the corner-bisector. It is clear from figure 18 that the turbulence activity is strongly reduced for $\phi = 0.2$. The probability of ejection and sweep events close to the walls is drastically reduced. The probability of sweep (Q4) events is around 35% only in a small region close to the wall bisector ($y/h \sim 0.85$). Instead, the probabilities of Q2 (ejections) and Q3 events are above 35% in a region around the corner bisector, where we recall there is high mean particle concentration ($y/h \in (0; 0.4)$). At this volume fraction the probability of these events is therefore mostly correlated to fluid-particle interactions. The probability contours for $\phi = 0.2$ are indeed very different from those at lower ϕ and from those of the unladen case. The absence of high probability regions of Q2 and Q4 events around $z/h \sim 0.8$ and $z/h \sim 0.3$ denotes the disruption of the coherent streamwise vortical structures.

The presence of two inhomogeneous directions allows us to extend the quadrant analysis to the secondary shear stress $\langle v'_f w'_f \rangle$, which contributes to the production, dissipation and transport of mean streamwise vorticity as discussed above. As in Huser & Biringen (1993), to distinguish between the events related to the primary and secondary Reynolds stresses, we will refer to the latter as $Q1_s$, $Q2_s$, $Q3_s$ and $Q4_s$ events. These authors showed that as the corners are approached, contributions of the $Q1_s$ and $Q3_s$ events progressively decrease. On the other hand, $Q2_s$ and $Q4_s$ events are found to be stronger than the latter close to the corners. This is due to the interaction between ejections from both walls that tilt the ejection stem toward the perpendicular wall. We looked at probability maps of these events as previously done for the events related to the primary Reynolds stress. For the unladen case we see indeed that close to the corners the probability of having $Q2_s$ and $Q4_s$ events is substantially larger than that of $Q1_s$, $Q3_s$ events (not shown). As we increase the volume fraction ϕ the probability of these events remains high until the highest $\phi = 0.2$ is reached. In this case, we find that there is an approximately equal share of probability between all type of events indicating again that there is a substantial alteration of the turbulence and less structured flow in the presence of many particles.

To further understand the effect of the solid particles on the turbulence features we report in figure 19 the two-point autocorrelations of streamwise and wall-normal velocities

along the spanwise direction

$$R_{uu}(y, \Delta z) = \frac{\langle u'(x, y, z, t) u'(x, y, z + \Delta z, t) \rangle}{u_{rms}^2} \quad (3.5)$$

$$R_{vv}(y, \Delta z) = \frac{\langle v'(x, y, z, t) v'(x, y, z + \Delta z, t) \rangle}{v_{rms}^2}. \quad (3.6)$$

These are shown at two wall-normal distances corresponding to 1 and 2 particles diameters ($y = 2a \simeq 20\delta_*$ and $y = 4a \simeq 40\delta_*$) in figures 19(a,c) and figures 19(b,d), respectively. The correlations are here calculated for the combined phase, and Δz is normalized by the viscous length at the wall-bisector.

It is well-known that for single-phase turbulent flows these correlations exhibit negative minimum values in the near-wall region and that the corresponding Δz^+ is indicative of the width of the typical structures of wall-bounded turbulence that sustain the turbulence process (i.e. quasi-streamwise vortices and low-speed streaks, Kim *et al.* 1987; Waleffe 1997; Pope 2000). The streamwise autocorrelation R_{uu} evaluated at $y = 2a \simeq 20\delta_*$, see figure 19(a), reveals that the minimum is smoothed with ϕ , while the separation distance increases. The smoothening of the minimum indicates that the width of the near-wall structures is less evident. Also at $y = 4a \simeq 40\delta_*$, figure 19(b), the separation distance increases with ϕ . However, we also see that the minimum value decreases with the volume fraction with $\phi = 0.1$. Hence, at this distance from the wall it is possible to identify wider streamwise velocity streaks with respect to those of the unladen case.

The autocorrelation of the wall-normal velocity fluctuations at the same wall-normal locations, are instead shown in figure 19(c) and (d). The data show that the negative minima of the unladen case progressively disappears by increasing solid volume fraction ϕ . Therefore, as ϕ increases, the turbulence structures become less organised in coherent structures as also observed by Picano *et al.* (2015) for channel flow.

4. Final remarks

We have studied turbulent duct flows laden with suspensions of finite-size particles, particles larger than the smallest flow structures. We have considered neutrally-buoyant rigid spheres of size $a = h/18 \sim 10\delta_*$ and three solid volume fractions $\phi = 0.05, 0.1, 0.2$. The bulk Reynolds number has been set to $Re_b = 5600$ to compare results with those found for turbulent channel flow of similar h/a and Re_b . For the unladen duct, this choice of Re_b results in a mean friction Reynolds number $Re_\tau = 185$ and friction factor of 0.035 (same value that is obtained via the empirical formula of Jones 1976).

One of the main findings concerns the effect of the particle presence on the so-called secondary/cross-flow velocities of the fluid phase. In single-phase turbulent duct flows their magnitude is about 2% of the bulk velocity. We have found that the intensity of these secondary flows progressively increases with solid volume fraction up to $\phi = 0.1$. Above this volume fraction, a strong turbulence activity attenuation is found and correspondingly the maximum value of the cross-flow velocity magnitude sharply drops below the value of the unladen case. Interestingly, we have found a lag between fluid and particle cross-flow velocities. In particular, at the corner bisectors the fluid cross-flow velocity is larger than that of the solid phase. On the contrary, the fluid and particle cross-flow velocities are similar at the walls away from the corners. It is well-known that at the wall-bisectors these secondary flows convect low-momentum fluid from the walls towards the duct core. This induces a convexity in the mean fluid streamwise velocity isotach (i.e. at equal distance from the walls, the mean streamwise velocity is larger at the corner-bisector than at the wall-bisector). As the cross-flow velocity increases with ϕ , so

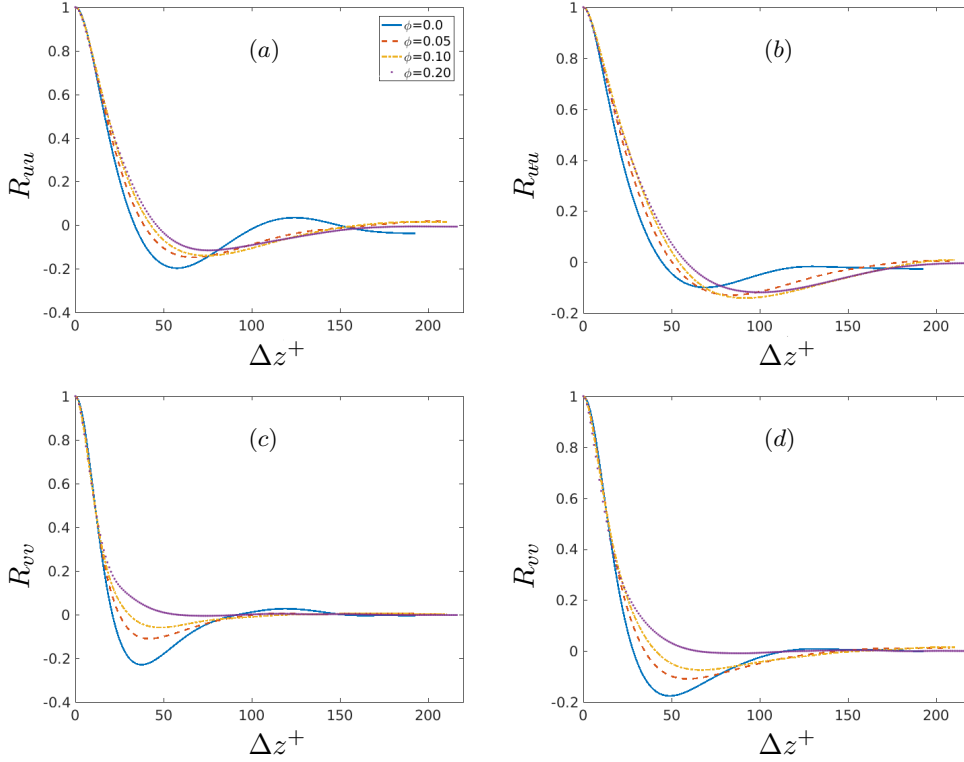


FIGURE 19. Two-point correlations of the velocity fluctuations versus the spanwise separation Δz^+ for all ϕ . Streamwise-streamwise component R_{uu} at (a) $y = 2a = h/9 \simeq 20\delta_*$ and (b) $y = 4a = 2h/9 \simeq 40\delta_*$ (a is the particle radius). Wall-normal component R_{vv} at (c) $y = a = h/9 \simeq 20\delta_*$ and (d) $y = 4a = 2h/9 \simeq 40\delta_*$.

does the convexity of the mean streamwise velocity contours. For $\phi = 0.2$ the convexity is less than in the unladen case. For all ϕ , the mean streamwise velocity of the solid phase is similar to that of the fluid, except very close to the walls where the particle velocity is not subjected to the no-slip condition.

At the wall-bisector, the mean streamwise velocity profiles are found to be similar to those in channel flows. In particular, as ϕ increases, the velocity decreases closer to the walls and increases towards the core. For $\phi = 0.2$ we have found a more abrupt increase in velocity than what was previously found in channel flows. We have also reported the mean streamwise velocity in inner units and calculated the von Kármán constant, κ , and the additive coefficient B . For the unladen case we have obtained the same κ found by Gavrilakis (1992) for $Re_b = 4410$. Increasing ϕ both κ and B are found to decrease denoting a contrasting behavior in terms of drag reduction or enhancement. The friction Reynolds number calculated at the wall-bisector, $Re_{\tau,bis}$ is found to increase for all ϕ , as in channel flow, although the increase is smaller than in the latter flow case at equal ϕ . Interestingly, for $\phi = 0.1$ the mean Re_τ and that calculated at the bisector almost coincide and, for larger ϕ the mean Re_τ is then found to decrease. Hence, the importance of particle-induced stresses on the overall drag is less in a more realistic geometry such as the one studied here, compared to channel flow.

Other important observations concern the mean particle concentration. Particles tend to form a stable layer very close to the walls for all ϕ . However, for $\phi \leq 0.1$, the higher

particle concentration is on the corner-bisectors close to the corner (at a distance of about $0.27h$). The high particle concentration at the corners is probably related to the existence of the secondary flows. Eventually, it results from the observed lag between the fluid and solid phases cross-flow velocities. It should be noted that in laminar duct flows of similar h/a and $Re_b \sim 500$ particles are also found to mostly accumulate at the corners (Kazerooni *et al.* 2017). In the latter case this is a result of the particle inertial migration away from the duct core. For $\phi = 0.2$, the particle concentration close to the corners is still high, but the maximum concentration is found at the duct core. This observation is in contrast to what found in channel flow, revealing the importance of confinement on particle dynamics. From the data available for channel flow, we have indeed found that there is a substantial number of particles crossing the periodic boundaries (i.e. a significant particle diffusion in the spanwise direction). The additional confinement due to the vertical walls induces therefore a different particle concentration.

Examining the fluid and particles velocity fluctuations, we see that close to the walls there is a redistribution of energy towards a more isotropic state (i.e. decrease of the streamwise r.m.s. velocity with ϕ and an increase of the fluctuation velocities in the cross-stream directions). For $\phi = 0.2$ all components of the r.m.s. velocity are found to be smaller than those of the unladen case, except for the spanwise and wall-normal components close to the corners. Looking at the primary Reynolds stress, we have seen that it increases throughout the cross-section up to $\phi = 0.1$. It is interesting to note that for turbulent channel flow, Picano *et al.* (2015) found that the maximum $\langle u'_f v'_f \rangle^+$ decreases with ϕ . On the other hand, we have here found that at the wall-bisector the maximum is approximately constant up to $\phi = 0.1$. So the turbulence activity reduction becomes important for volume fractions larger than $\phi = 0.1$ as can be seen from the results obtained for $\phi = 0.2$.

Interestingly, close to the corners the secondary Reynolds stress $\langle v'_f w'_f \rangle$, is larger than in the single-phase case for all ϕ . The secondary Reynolds stress of the solid phase, $\langle v'_p w'_p \rangle$, resemble those of the fluid, except at the corners where they change sign. Therefore they may represent an additional source of mean streamwise vorticity. Indeed, close to the corners and in the viscous sublayer, the gradients of the fluid secondary Reynolds stress typically act as a sink of mean streamwise vorticity (the production of vorticity within the viscous sublayer is mainly responsible for the presence of vorticity in the bulk of the flow). The opposite sign may indicate that this new contribution due to the solid phase actually acts as a source term.

Finally, we have performed quadrant analyses of both primary and secondary Reynolds stresses, looking at the occurrence probability of Q1, Q2, Q3 and Q4 events in the cross-section. The probabilities are everywhere similar up to $\phi = 0.1$, again indicating that the turbulence is not strongly altered up to this solid volume fraction. However, for $\phi = 0.2$ the probability maps change drastically denoting a strong reduction of the turbulence activity. The velocity autocorrelations confirm these results as for the largest ϕ the typical negative minima disappear, denoting a weaker organisation of the turbulence in coherent structures.

This work was supported by the European Research Council Grant No. ERC-2013-CoG-616186, TRITOS. Computer time was provided by SNIC (Swedish National Infrastructure for Computing). The Authors also acknowledge the support from the COST Action MP1305: *Flowing matter*.

REFERENCES

- ABBAS, M, MAGAUD, P, GAO, Y & GEOFFROY, S 2014 Migration of finite sized particles in a laminar square channel flow from low to high Reynolds numbers. *Physics of Fluids (1994-present)* **26** (12), 123301.
- AMINI, HAMED, SOLLIER, ELODIE, WEAVER, WESTBROOK M & DI CARLO, DINO 2012 Intrinsic particle-induced lateral transport in microchannels. *Proceedings of the National Academy of Sciences* **109** (29), 11593–11598.
- ARDEKANI, M NIAZI, COSTA, PEDRO, BREUGEM, W-P, PICANO, FRANCESCO & BRANDT, LUCA 2017 Drag reduction in turbulent channel flow laden with finite-size oblate spheroids. *Journal of Fluid Mechanics* **816**, 43–70.
- BALACHANDAR, S & EATON, JOHN K 2010 Turbulent dispersed multiphase flow. *Annual Review of Fluid Mechanics* **42**, 111–133.
- BRENNER, HOWARD 1961 The slow motion of a sphere through a viscous fluid towards a plane surface. *Chemical engineering science* **16** (3-4), 242–251.
- BREUGEM, WP & BOERSMA, BJ 2005 Direct numerical simulations of turbulent flow over a permeable wall using a direct and a continuum approach. *Physics of Fluids (1994-present)* **17** (2), 025103.
- BREUGEM, WIM-PAUL 2012 A second-order accurate immersed boundary method for fully resolved simulations of particle-laden flows. *Journal of Computational Physics* **231** (13), 4469–4498.
- BREUGEM, WIM-PAUL, VAN DIJK, VINCENT & DELFOS, RENÉ 2014 Flows through real porous media: X-ray computed tomography, experiments, and numerical simulations. *Journal of Fluids Engineering* **136** (4), 040902.
- CHUN, B & LADD, AJC 2006 Inertial migration of neutrally buoyant particles in a square duct: An investigation of multiple equilibrium positions. *Physics of Fluids (1994-present)* **18** (3), 031704.
- COSTA, PEDRO, BOERSMA, BENDIKS JAN, WESTERWEEL, JERRY & BREUGEM, WIM-PAUL 2015 Collision model for fully resolved simulations of flows laden with finite-size particles. *Physical Review E* **92** (5), 053012.
- COSTA, PEDRO, PICANO, FRANCESCO, BRANDT, LUCA & BREUGEM, WIM-PAUL 2016 Universal scaling laws for dense particle suspensions in turbulent wall-bounded flows. *Physical Review Letters* **117** (13), 134501.
- DOYEUX, VINCENT, PRIEM, STEPHANE, JIBUTI, LEVAN, FARUTIN, ALEXANDER, ISMAIL, MOURAD & PEYLA, PHILIPPE 2016 Effective viscosity of two-dimensional suspensions: Confinement effects. *Physical Review Fluids* **1** (4), 043301.
- FORNARI, WALTER, BRANDT, LUCA, CHAUDHURI, PINAKI, LOPEZ, CYAN UMBERT, MITRA, DHRUBADITYA & PICANO, FRANCESCO 2016a Rheology of confined non-brownian suspensions. *Physical Review Letters* **116** (1), 018301.
- FORNARI, WALTER, FORMENTI, ALBERTO, PICANO, FRANCESCO & BRANDT, LUCA 2016b The effect of particle density in turbulent channel flow laden with finite size particles in semi-dilute conditions. *Physics of Fluids (1994-present)* **28** (3), 033301.
- FORNARI, WALTER, PICANO, FRANCESCO & BRANDT, LUCA 2016c Sedimentation of finite-size spheres in quiescent and turbulent environments. *Journal of Fluid Mechanics* **788**, 640–669.
- FORNARI, WALTER, PICANO, FRANCESCO & BRANDT, LUCA 2018 The effect of polydispersity in a turbulent channel flow laden with finite-size particles. *European Journal of Mechanics - B/Fluids* **67**, 54 – 64.
- GAVRILAKIS, S 1992 Numerical simulation of low-Reynolds-number turbulent flow through a straight square duct. *Journal of Fluid Mechanics* **244**, 101–129.
- GESSNER, FB 1973 The origin of secondary flow in turbulent flow along a corner. *Journal of Fluid Mechanics* **58** (01), 1–25.
- GUAZZELLI, ELISABETH & MORRIS, JEFFREY F 2011 *A physical introduction to suspension dynamics*, , vol. 45. Cambridge University Press.
- HENNINGSON, DAN S & KIM, JOHN 1991 On turbulent spots in plane poiseuille flow. *Journal of fluid mechanics* **228**, 183–205.
- HUSER, ASMUND & BIRINGEN, SEDAT 1993 Direct numerical simulation of turbulent flow in a square duct. *Journal of Fluid Mechanics* **257**, 65–95.
- JONES, OC 1976 An improvement in the calculation of turbulent friction in rectangular ducts. *Journal of Fluids Engineering* **98** (2), 173–180.

- JOUNG, YOUNGHOON, CHOI, SUNG-UK & CHOI, JUNG-IL 2007 Direct numerical simulation of turbulent flow in a square duct: analysis of secondary flows. *Journal of engineering mechanics* **133** (2), 213–221.
- KAZEROONI, H. TABAEI, FORNARI, W., HUSSONG, J. & BRANDT, L. 2017 Inertial migration in dilute and semidilute suspensions of rigid particles in laminar square duct flow. *Physical Review Fluids* **2**, 084301.
- KIM, JOHN, MOIN, PARVIZ & MOSER, ROBERT 1987 Turbulence statistics in fully developed channel flow at low Reynolds number. *Journal of fluid mechanics* **177**, 133–166.
- KOH, CHRISTOPHER J, HOOKHAM, PHILIP & LEAL, LG 1994 An experimental investigation of concentrated suspension flows in a rectangular channel. *Journal of Fluid Mechanics* **266**, 1–32.
- KULICK, JONATHAN D, FESSLER, JOHN R & EATON, JOHN K 1994 Particle response and turbulence modification in fully developed channel flow. *Journal of Fluid Mechanics* **277** (1), 109–134.
- KULKARNI, P.M. & MORRIS, J.F. 2008 Suspension properties at finite Reynolds number from simulated shear flow. *Phys. Fluids* **20** (040602).
- LASHGARI, IMAN, ARDEKANI, MEHDI NIAZI, BANERJEE, INDRADUMNA, RUSSOM, AMAN & BRANDT, LUCA 2017a Inertial migration of spherical and oblate particles in straight ducts. *Journal of Fluid Mechanics* **819**, 540–561.
- LASHGARI, IMAN, PICANO, FRANCESCO & BRANDT, LUCA 2015 Transition and self-sustained turbulence in dilute suspensions of finite-size particles. *Theoretical and Applied Mechanics Letters* .
- LASHGARI, IMAN, PICANO, FRANCESCO, BREUGEM, WIM-PAUL & BRANDT, LUCA 2014 Laminar, turbulent, and inertial shear-thickening regimes in channel flow of neutrally buoyant particle suspensions. *Physical Review Letters* **113** (25), 254502.
- LASHGARI, IMAN, PICANO, FRANCESCO, BREUGEM, WIM PAUL & BRANDT, LUCA 2016 Channel flow of rigid sphere suspensions: Particle dynamics in the inertial regime. *International Journal of Multiphase Flow* **78**, 12–24.
- LASHGARI, IMAN, PICANO, FRANCESCO, COSTA, PEDRO, BREUGEM, WIM-PAUL & BRANDT, LUCA 2017b Turbulent channel flow of a dense binary mixture of rigid particles. *Journal of Fluid Mechanics* **818**, 623–645.
- LIN, ZHAO-WU, SHAO, XUE-MING, YU, ZHAO-SHENG & WANG, LIAN-PING 2017 Effects of finite-size heavy particles on the turbulent flows in a square duct. *Journal of Hydrodynamics, Ser. B* **29** (2), 272–282.
- LOISEL, VINCENT, ABBAS, MICHELINE, MASBERNAT, OLIVIER & CLIMENT, ERIC 2013 The effect of neutrally buoyant finite-size particles on channel flows in the laminar-turbulent transition regime. *Physics of Fluids (1994-present)* **25** (12), 123304.
- MATAS, J-P, MORRIS, JEFFREY F & GUAZZELLI, E 2003 Transition to turbulence in particulate pipe flow. *Physical Review Letters* **90** (1), 014501.
- MATAS, JEAN-PHILIPPE, MORRIS, JEFFREY F & GUAZZELLI, ÉLISABETH 2004 Inertial migration of rigid spherical particles in poiseuille flow. *Journal of Fluid Mechanics* **515**, 171–195.
- MAXEY, MARTIN 2017 Simulation methods for particulate flows and concentrated suspensions. *Annual Review of Fluid Mechanics* **49**, 171–193.
- MORITA, YUSUKE, ITANO, TOMOAKI & SUGIHARA-SEKI, MASAKO 2017 Equilibrium radial positions of neutrally buoyant spherical particles over the circular cross-section in poiseuille flow. *Journal of Fluid Mechanics* **813**, 750–767.
- MORRIS, JEFFREY F 2009 A review of microstructure in concentrated suspensions and its implications for rheology and bulk flow. *Rheologica acta* **48** (8), 909–923.
- MORRIS, J. F. & HADDADI, H. 2014 Microstructure and rheology of finite inertia neutrally buoyant suspensions. *Journal of Fluid Mechanics* **749**, 431–459.
- NAKAGAWA, NAOTO, YABU, TAKUYA, OTOMO, RYOKO, KASE, ATSUSHI, MAKINO, MASATO, ITANO, TOMOAKI & SUGIHARA-SEKI, MASAKO 2015 Inertial migration of a spherical particle in laminar square channel flows from low to high Reynolds numbers. *Journal of Fluid Mechanics* **779**, 776.
- NOORANI, AZAD, VINUESA, RICARDO, BRANDT, LUCA & SCHLATTER, PHILIPP 2016 Aspect ratio effect on particle transport in turbulent duct flows. *Physics of Fluids* **28** (11), 115103.

- PICANO, FRANCESCO, BREUGEM, WIM-PAUL & BRANDT, LUCA 2015 Turbulent channel flow of dense suspensions of neutrally buoyant spheres. *Journal of Fluid Mechanics* **764**, 463–487.
- PICANO, FRANCESCO, BREUGEM, WIM-PAUL, MITRA, DHRUBADITYA & BRANDT, LUCA 2013 Shear thickening in non-brownian suspensions: an excluded volume effect. *Physical Review Letters* **111** (9), 098302.
- PINELLI, ALFREDO, UHLMANN, MARKUS, SEKIMOTO, ATSUSHI & KAWAHARA, GENTA 2010 Reynolds number dependence of mean flow structure in square duct turbulence. *Journal of fluid mechanics* **644**, 107–122.
- POPE, STEPHEN B 2000 *Turbulent flows*. Cambridge university press.
- POURQUIE, MBJM, BREUGEM, WP & BOERSMA, BENDIKS JAN 2009 Some issues related to the use of immersed boundary methods to represent square obstacles. *International Journal for Multiscale Computational Engineering* **7** (6).
- PRANDTL, LUDWIG 1963 *The essentials of fluid dynamics*. Blackie & Son Limited.
- REEKS, MW 1983 The transport of discrete particles in inhomogeneous turbulence. *Journal of aerosol science* **14** (6), 729–739.
- SAMANTA, ARGHYA, VINUESA, RICARDO, LASHGARI, IMAN, SCHLATTER, PHILIPP & BRANDT, LUCA 2015 Enhanced secondary motion of the turbulent flow through a porous square duct. *Journal of Fluid Mechanics* **784**, 681–693.
- SARDINA, GAETANO, PICANO, FRANCESCO, SCHLATTER, PHILIPP, BRANDT, LUCA & CASCIOLA, CARLO MASSIMO 2011 Large scale accumulation patterns of inertial particles in wall-bounded turbulent flow. *Flow, turbulence and combustion* **86** (3-4), 519–532.
- SARDINA, G, SCHLATTER, PHILIPP, BRANDT, LUCA, PICANO, F & CASCIOLA, CM 2012 Wall accumulation and spatial localization in particle-laden wall flows. *Journal of Fluid Mechanics* **699**, 50–78.
- SEGRE, G & SILBERBERG, A 1962 Behaviour of macroscopic rigid spheres in poiseuille flow part 2. experimental results and interpretation. *Journal of Fluid Mechanics* **14** (01), 136–157.
- SHARMA, GAURAV & PHARES, DENIS J 2006 Turbulent transport of particles in a straight square duct. *International Journal of Multiphase Flow* **32** (7), 823–837.
- SOLDATI, ALFREDO & MARCHIOLI, CRISTIAN 2009 Physics and modelling of turbulent particle deposition and entrainment: Review of a systematic study. *International Journal of Multiphase Flow* **35** (9), 827–839.
- STICKEL, JONATHAN J & POWELL, ROBERT L 2005 Fluid mechanics and rheology of dense suspensions. *Annual Review of Fluid Mechanics* **37**, 129–149.
- UHLMANN, MARKUS 2005 An immersed boundary method with direct forcing for the simulation of particulate flows. *Journal of Computational Physics* **209** (2), 448–476.
- VINUESA, RICARDO, NOORANI, AZAD, LOZANO-DURÁN, ADRIÁN, KHOURY, GEORGE K EL, SCHLATTER, PHILIPP, FISCHER, PAUL F & NAGIB, HASSAN M 2014 Aspect ratio effects in turbulent duct flows studied through direct numerical simulation. *Journal of Turbulence* **15** (10), 677–706.
- VIRK, PREETINDER S 1975 Drag reduction fundamentals. *AIChE Journal* **21** (4), 625–656.
- WAGNER, NORMAN J & BRADY, JOHN F 2009 Shear thickening in colloidal dispersions. *Physics Today* **62** (10), 27–32.
- WALEFFE, FABIAN 1997 On a self-sustaining process in shear flows. *Physics of Fluids* **9** (4), 883–900.
- WINKLER, CM, RANI, SARMA L & VANKA, SP 2004 Preferential concentration of particles in a fully developed turbulent square duct flow. *International Journal of Multiphase Flow* **30** (1), 27–50.
- ZHAO, LH, ANDERSSON, HELGE I & GILLISSEN, JJJ 2010 Turbulence modulation and drag reduction by spherical particles. *Physics of Fluids (1994-present)* **22** (8), 081702.